

Nuclear structure and elastic scattering observables obtained consistently with different NN interactions

R. B. Baker,¹ M. Burrows,² Ch. Elster,¹ P. Maris,³ G. Popa,¹ and S. P. Weppner⁴

¹*Institute of Nuclear and Particle Physics, and Department of Physics and Astronomy, Ohio University, Athens, OH 45701, USA*

²*Department of Physics and Astronomy, Louisiana State University, Baton Rouge, LA 70803, USA*

³*Department of Physics and Astronomy, Iowa State University, Ames, IA 50011, USA*

⁴*Natural Sciences, Eckerd College, St. Petersburg, FL 33711, USA*

(Dated: June 23, 2023)

Nucleon-nucleon (NN) interactions based on chiral effective theories are commonly used in *ab initio* calculations of light nuclei. Here we present a study based on three different NN interactions (up to next-to-next-to-leading order) for which structure and elastic proton scattering observables are consistently calculated for ${}^4\text{He}$, ${}^{12}\text{C}$, and ${}^{16}\text{O}$. The interactions are compared at the two-body level in terms of Wolfenstein amplitudes, and their predictions for ground state energies, point-proton radii, and charge form factors, as well as proton elastic scattering observables in the leading-order spectator expansion in the energy range between 65 and 160 MeV projectile energy are presented. To gain further insight into differences visible in elastic scattering observables, we investigate the behavior of the calculated effective nucleon-nucleus interactions for the ${}^{12}\text{C}$ nucleus based on the different NN interactions.

I. INTRODUCTION

Over the last decade developments of the nucleon-nucleon (NN) and three-nucleon ($3N$) interactions derived from chiral effective field theory have yielded major progress [1–8]. They, together with the utilization of massively parallel computing resources (e.g., see [9–13]), have placed *ab initio* large-scale simulations at the frontier of nuclear structure and reaction explorations. Among other successful many-body theories, the *ab initio* no-core shell model (NCSM) approach (see, e.g., [14–17]), has over the last decade taken center stage in the development of microscopic tools for studying the structure of atomic nuclei up to $A \simeq 16$.

Following the developments in *ab initio* structure theory, rigorous calculations of effective folding nucleon-nucleus (NA) interactions for elastic scattering of protons or neutrons from nuclei in the same mass region were developed [18–25] based on the leading-order in the spectator expansion of multiple scattering theory [26–28]. Here the nuclear one-body densities that are required for the folding with NN scattering amplitudes can be based on the same chiral NN interaction. This development not only allows one to consider NA effective interaction derived in leading-order of the spectator expansion as *ab initio*, but also allows an investigation of effects of truncation uncertainties in the chiral expansion on NA scattering observables in a similar fashion as already successfully performed in NN scattering (see e.g. [29–31]), nucleon-deuteron scattering [32], or structure observables for light nuclei [17, 33].

To date there is no unambiguous description of the strong interaction between nucleons based on effective field theories. Most strikingly, it is not fully understood why some descriptions of the nuclear interaction based on this framework and calibrated to reproduce similar data in the few-nucleon sector do better than others in predicting fundamental nuclear quantities such as binding energies, radii, decays, or cross sections. Though this work will not be able to answer those questions, our aim is to illustrate those differences by looking at structure and elastic scattering observables simultaneously. For our study we choose three different NN interactions based on chiral effective theory at next-to-next-to-leading order, which are calibrated to NN data.

The construction of the effective NA interaction in leading order in the spectator expansion is briefly reviewed in Section II to introduce how the NN interaction enters the elastic scattering calculations. Then the three different interactions based on chiral effective theory, namely the NNLO_{opt} [34] and the EKM [4, 5] chiral interactions as well as the Daejeon16 potential [35], are introduced together with NN amplitudes which are relevant for the construction of the effective NA interaction. Section III considers structure observables for ${}^4\text{He}$, ${}^{12}\text{C}$, and ${}^{16}\text{O}$ predicted from those interactions, as well as the charge form factors, as experimentally extracted from elastic electron-nucleus scattering. In Section IV proton-nucleus elastic scattering from those nuclei in the energy range from 65 to 160 MeV laboratory kinetic energy are presented. Effective NA interactions are in general nonlocal as well as energy dependent. In order to gain insight into their structure and enable a connection to phenomenological local optical potentials we extract in Section V the local part and parameterize it with traditional Woods-Saxon forms in the appendix. We conclude in Section VI.

II. AB INITIO EFFECTIVE NA INTERACTIONS

Calculating elastic nucleon-nucleus scattering observables in an *ab initio* fashion requires the interaction between the projectile and the nucleons in the target, as well as the interaction between the nucleons within the target. A multiple scattering expansion can organize the interactions between the projectile and the nucleons in the target according to the number of active nucleons participating in the reaction, as is done e.g. in the spectator expansion [26, 36, 37]. The structure of the target nucleus is calculated employing *ab initio* many-body methods. For this work we are using the no-core shell model (NCSM) [16], which is well-suited for light nuclei; more details about the nuclear structure calculation are given in Section III below.

Up to now the leading order in the spectator expansion, which implies two active nucleons, has been evaluated *ab initio* in several works for elastic scattering of protons (neutrons) from nuclei with a 0^+ ground state [19, 22] as well as nuclei with $J^\pi \neq 0^+$ [23]. In this work we concentrate on proton scattering from light nuclei with $J^\pi = 0^+$ in leading order in the spectator expansion. In this case the effective interaction of the projectile proton with a single target nucleon can be written as function of the momentum transfer \mathbf{q} and the average momentum \mathcal{K}_{NA} , where the subscript NA refers to the nucleon-nucleus (NA) frame.

$$\begin{aligned}
\widehat{U}_p(\mathbf{q}, \mathcal{K}_{NA}; \epsilon) = & \\
& \sum_{\alpha=n,p} \int d^3\mathcal{K} \eta(\mathbf{q}, \mathcal{K}, \mathcal{K}_{NA}) A_{p\alpha} \left(\mathbf{q}, \frac{1}{2} \left(\frac{A+1}{A} \mathcal{K}_{NA} - \mathcal{K} \right); \epsilon \right) \rho_\alpha^{K_s=0}(\mathcal{P}', \mathcal{P}) \\
& + i(\boldsymbol{\sigma}^{(0)} \cdot \hat{\mathbf{n}}) \sum_{\alpha=n,p} \int d^3\mathcal{K} \eta(\mathbf{q}, \mathcal{K}, \mathcal{K}_{NA}) C_{p\alpha} \left(\mathbf{q}, \frac{1}{2} \left(\frac{A+1}{A} \mathcal{K}_{NA} - \mathcal{K} \right); \epsilon \right) \rho_\alpha^{K_s=0}(\mathcal{P}', \mathcal{P}) \\
& + i \sum_{\alpha=n,p} \int d^3\mathcal{K} \eta(\mathbf{q}, \mathcal{K}, \mathcal{K}_{NA}) C_{p\alpha} \left(\mathbf{q}, \frac{1}{2} \left(\frac{A+1}{A} \mathcal{K}_{NA} - \mathcal{K} \right); \epsilon \right) S_{n,\alpha}(\mathcal{P}', \mathcal{P}) \cos \beta \\
& + i(\boldsymbol{\sigma}^{(0)} \cdot \hat{\mathbf{n}}) \sum_{\alpha=n,p} \int d^3\mathcal{K} \eta(\mathbf{q}, \mathcal{K}, \mathcal{K}_{NA}) (-i) M_{p\alpha} \left(\mathbf{q}, \frac{1}{2} \left(\frac{A+1}{A} \mathcal{K}_{NA} - \mathcal{K} \right); \epsilon \right) S_{n,\alpha}(\mathcal{P}', \mathcal{P}) \cos \beta, \quad (1)
\end{aligned}$$

where the subscript p indicates the projectile being a proton. The energy ϵ is taken in the impulse approximation as half of the projectile energy. The momentum vectors in the problem are given as

$$\begin{aligned}
\mathbf{q} &= \mathbf{p}' - \mathbf{p} = \mathbf{k}' - \mathbf{k}, \\
\mathcal{K} &= \frac{1}{2}(\mathbf{p}' + \mathbf{p}), \\
\hat{\mathbf{n}} &= \frac{\mathcal{K} \times \mathbf{q}}{|\mathcal{K} \times \mathbf{q}|} \\
\mathcal{K}_{NA} &= \frac{A}{A+1} \left[(\mathbf{k}' + \mathbf{k}) + \frac{1}{2}(\mathbf{p}' + \mathbf{p}) \right], \\
\mathcal{P} &= \mathcal{K} + \frac{A-1}{A} \frac{\mathbf{q}}{2}, \\
\mathcal{P}' &= \mathcal{K} - \frac{A-1}{A} \frac{\mathbf{q}}{2}. \quad (2)
\end{aligned}$$

The momentum of the incoming proton is given by \mathbf{k} , its outgoing momentum by \mathbf{k}' , the momentum transfer by \mathbf{q} , and the average momentum \mathcal{K}_{NA} . The struck nucleon in the target has an initial momentum \mathbf{p} and a final momentum \mathbf{p}' . The two quantities representing the structure of the nucleus are the scalar one-body density $\rho_\alpha^{K_s=0}(\mathcal{P}', \mathcal{P})$ and the spin-projected momentum distribution $S_{n,\alpha}(\mathcal{P}', \mathcal{P})$. Both distributions are nonlocal and translationally invariant. Lastly, the term $\cos \beta$ in Eq. (1) comes from projecting $\hat{\mathbf{n}}$ from the NN frame to the NA frame. For further details see Ref. [19]. The term $\eta(\mathbf{q}, \mathcal{K}, \mathcal{K}_{NA})$ is the Møller factor [38] describing the transformation from the NN frame to the NA frame.

When calculating NA elastic scattering amplitudes, the leading order term of Eq. (1) does not directly enter a Lippmann-Schwinger type integral equation. To obtain the Watson optical potential $U_p(\mathbf{q}, \mathcal{K}_{NA}; \epsilon)$, an additional integral equation needs to be solved [18, 37],

$$U_p = \widehat{U}_p - \widehat{U}_p G_0(E) P U_p, \quad (3)$$

where for simplicity the momentum variables are omitted. Here $G_0(E)$ is the free NA propagator and P a projector on the ground state.

The functions $A_{p\alpha}$, $C_{p\alpha}$, and $M_{p\alpha}$ represent the NN interaction through Wolfenstein amplitudes (see discussion below). Since the incoming proton can interact with either a proton or a neutron in the nucleus, the index α indicates

the neutron (n) and proton (p) contributions, which are calculated separately and then summed up. With respect to the nucleus, the operator $i(\boldsymbol{\sigma}^{(0)} \cdot \hat{\mathbf{n}})$ represents the spin-orbit operator in momentum space of the projectile. As such, Eq. (1) exhibits the expected form of an interaction between a spin- $\frac{1}{2}$ projectile and a target nucleus in a $J = 0$ state [39].

The effective NA interaction in the leading order spectator expansion is driven by the NN amplitude, which in its most general form can be parameterized in terms of Wolfenstein amplitudes [40–42],

$$\begin{aligned}
\overline{M}(\mathbf{q}, \mathcal{K}_{NN}, \epsilon) &= A(\mathbf{q}, \mathcal{K}_{NN}, \epsilon) \mathbf{1} \otimes \mathbf{1} \\
&+ iC(\mathbf{q}, \mathcal{K}_{NN}, \epsilon) \left(\boldsymbol{\sigma}^{(0)} \cdot \hat{\mathbf{n}} \right) \otimes \mathbf{1} \\
&+ iC(\mathbf{q}, \mathcal{K}_{NN}, \epsilon) \mathbf{1} \otimes \left(\boldsymbol{\sigma}^{(i)} \cdot \hat{\mathbf{n}} \right) \\
&+ M(\mathbf{q}, \mathcal{K}_{NN}, \epsilon) (\boldsymbol{\sigma}^{(0)} \cdot \hat{\mathbf{n}}) \otimes (\boldsymbol{\sigma}^{(i)} \cdot \hat{\mathbf{n}}) \\
&+ [G(\mathbf{q}, \mathcal{K}_{NN}, \epsilon) - H(\mathbf{q}, \mathcal{K}_{NN}, \epsilon)] (\boldsymbol{\sigma}^{(0)} \cdot \hat{\mathbf{q}}) \otimes (\boldsymbol{\sigma}^{(i)} \cdot \hat{\mathbf{q}}) \\
&+ [G(\mathbf{q}, \mathcal{K}_{NN}, \epsilon) + H(\mathbf{q}, \mathcal{K}_{NN}, \epsilon)] (\boldsymbol{\sigma}^{(0)} \cdot \hat{\mathcal{K}}) \otimes (\boldsymbol{\sigma}^{(i)} \cdot \hat{\mathcal{K}}) \\
&+ D(\mathbf{q}, \mathcal{K}_{NN}, \epsilon) \left[(\boldsymbol{\sigma}^{(0)} \cdot \hat{\mathbf{q}}) \otimes (\boldsymbol{\sigma}^{(i)} \cdot \hat{\mathcal{K}}) + (\boldsymbol{\sigma}^{(0)} \cdot \hat{\mathcal{K}}) \otimes (\boldsymbol{\sigma}^{(i)} \cdot \hat{\mathbf{q}}) \right], \tag{4}
\end{aligned}$$

where $\boldsymbol{\sigma}^{(0)}$ describes the spin of the projectile, and $\boldsymbol{\sigma}^{(i)}$ the spin of the struck nucleon. The average momentum in the NN frame is defined as $\mathcal{K}_{NN} = \frac{1}{2}(\mathbf{k}'_{NN} + \mathbf{k}_{NN})$. The scalar functions A , C , M , G , H , and D are referred to as Wolfenstein amplitudes, and only depend on the scattering momenta and the energy, and are calculated for np and pp scattering respectively. The amplitude $D(\mathbf{q}, \mathcal{K}_{NN}, \epsilon)$ vanishes on-shell due to parity invariance. Each term in Eq. (4) is described by two components, namely a scalar function of two vector momenta and an energy (for NN scattering this is the c. m. energy of the NN system), and the coupling between the operators of the projectile and the struck nucleon. The Wolfenstein amplitude A sums up all pieces of the central NN force, while C represents all pieces contributing to the spin-orbit force. The amplitudes M , G , and H sum up tensor force contributions.

For the struck target nucleon i the expectation values of the of the operators $\mathbf{1}$ and the scalar products of $\boldsymbol{\sigma}^{(i)}$ with the linear independent unit vectors $\hat{\mathbf{n}}$, $\hat{\mathbf{q}}$, and \mathcal{K}_{NN} need to be calculated for the leading order NA effective interaction of Eq. (1). Evaluating the expectation value of the operator $\mathbf{1}$ in the ground state of the nucleus results in the scalar nonlocal, translationally invariant one-body density $\rho_{\alpha}^{K_s=0}$ in Eq. (1). This has traditionally and very successfully been used as input to microscopic or *ab initio* calculations of leading order effective interactions [18, 22, 43–45]. The other operators from Eq. (2), namely $(\boldsymbol{\sigma}^{(i)} \cdot \hat{\mathbf{n}})$, $(\boldsymbol{\sigma}^{(i)} \cdot \hat{\mathbf{q}})$, and $(\boldsymbol{\sigma}^{(i)} \cdot \hat{\mathcal{K}})$ need to also be evaluated for a leading-order *ab initio* NA effective interaction, in which the NN interaction is treated on equal footing in the reaction and structure calculation. Due to parity invariance arguments only the terms proportional to $(\boldsymbol{\sigma}^{(i)} \cdot \hat{\mathbf{n}})$ do not vanish in the sum over α for $J^\pi = 0^+$ nuclei, leading to spin-projected non-local one-body density $S_{n,\alpha}$ in Eq. (1) [19, 46]. Thus the tensor contributions of the NN force only enter the leading order effective NA interaction through the Wolfenstein amplitude M as long as elastic scattering is considered.

For the study of NA observables calculated in leading order of the spectator expansion we choose three different chiral NN interactions. One is the optimized chiral NN interaction at the next-to-next-to-leading order NNLO_{opt} from Ref. [34]. This interaction is fitted with $\chi^2 \approx 1$ per degree of freedom for laboratory energies up to about 125 MeV. In the $A = 3, 4$ nucleon systems the contributions of the 3NFs are smaller than in most other parameterizations of chiral interactions. As a consequence, nuclear quantities like root-mean-square radii and electromagnetic transitions in light and intermediate-mass nuclei can be calculated reasonably well without invoking 3NFs [47, 48]. The second is the chiral NN interaction from Refs. [4, 5] (sometimes referred to as EKM) with a semi-local cutoff $R = 1.0$ fm which we consider up to next-to-next-to-leading order. This interaction has been employed in Ref. [21] to quantify truncation errors of the chiral EFT in NA observables. As third interaction we employ the Daejeon16 potential [35], which is based on the Idaho N3LO chiral interaction [49], which is SRG evolved with a flow parameter $\lambda = 1.5 \text{ fm}^{-1}$ and cast into a harmonic oscillator basis. In addition phase-equivalent transformations are employed in some partial waves to minimize the need for the explicit introduction of three- and higher-body forces [35].

All three chiral NN interaction listed above describe the np and pp phase shifts equally well for NN laboratory kinetic energies up about 150 MeV, with differences being in details. For the application in NA scattering the focus may better be directed toward considering the relevant Wolfenstein amplitudes that enter the NA effective interaction of Eq. (1). Since Wolfenstein amplitudes are complex functions, we consider in Fig. 1 the squares of the real and imaginary parts and sum over the np and pp contributions as is done in obtaining the NA effective interaction, and concentrate on the energy regime between 65 and 155 MeV laboratory kinetic energies. As guide to the eye we also include the corresponding quantity obtained from the high-precision Cd-Bonn potential [50], which fits NN data with $\chi^2 \approx 1$ up to 300 MeV. We focus on momentum transfers below 1.6 fm^{-1} , since the forward direction of the amplitude A can be directly related to the differential cross sections for NA scattering at low momentum

transfer (small angles) [21]. It is interesting to notice that while at the smallest energy (65 MeV) all three potential exhibit roughly the same central strength and agree with the Cd-Bonn calculation, when moving to higher energies the NNLO_{opt} becomes considerably weaker, specifically when extrapolating beyond the energy range included when fitting its low-energy constants. We should thus expect that those differences become visible in NA scattering observables.

The Wolfenstein amplitude C characterizes the spin-orbit force of the NN interaction and is depicted in Fig. 2 for three different NN laboratory energies as function of the momentum transfer. In general, this amplitude is much smaller in magnitude compared to A . We also see that here even at the lowest energy the NNLO_{opt} is slightly larger compared to the amplitudes extracted from the other two interactions. This trend increases as the energy increases, indicating that the NN spin-orbit force is slightly stronger in the NNLO_{opt} chiral interaction. The amplitudes C is the main contribution to the spin-orbit part of the NA effective interaction, Eq. (1), and thus it may be expected that its effect may be visible in the NA spin observables. For a more in depth discussion we refer to Section IV.

Tensor force contributions of the NN force are summed up in the Wolfenstein amplitudes M , G , and H . For NA scattering from a 0^+ target, only the amplitude M contributes to the spin-orbit part of the effective interaction. All three chiral interactions considered in this work give identical M amplitudes in the energy range considered and agree perfectly well with the amplitude extracted from the Cd-Bonn potential. A possible explanation may be that the tensor force contributions are determined quite well when fitting to deuteron properties. All NN chiral interactions considered here are fitted to deuteron properties. In addition, the effect of the tensor force contribution to NA spin-observables is quite small in case of scattering from 0^+ targets, as was shown in Ref. [19].

III. STRUCTURE OBSERVABLES

Before discussing our results for nucleon-nucleus scattering, let us first consider the results for the ground states of the three nuclei under consideration, ^4He , ^{12}C , and ^{16}O . We obtain the ground state energies and wavefunctions of these nuclei by employing the NCSM [16]. In this approach the A -body wavefunctions are expanded in Slater determinants of A single-particle wavefunctions which turns the A -body Schrödinger equation into an eigenvalue problem for the expansion coefficients, with the lowest eigenvalue being the ground state energy. For any finite basis expansion, the obtained eigenvalue, E , gives a strict upper bound for the energy in the complete, but infinite-dimensional basis, and the corresponding eigenvector gives an approximation to the A -body wavefunction. As one increases the basis size, the obtained eigenvalues E approach the exact eigenvalues for a given Hamiltonian.

Here we follow the standard practice to use a harmonic oscillator (HO) basis for the single-particle wavefunctions; for the many-body truncation we use a truncation on the total number of HO quanta, that is, a truncation on $\sum_i (2n_i + l_i)$ over all A nucleons, with n and l the radial and orbital quantum numbers. The actual truncation parameter N_{max} is defined as the total number of HO quanta above the minimal configuration for the ground state satisfying the Pauli principle. One of the reasons for using a HO basis, in combination with a many-body truncation on the total number of HO quanta, is that this leads to an exact factorization of the A -body wavefunction into a center-of-mass wavefunction and a relative wavefunction [51, 52]. We use the ground state wavefunction obtained in the NCSM to evaluate the nonlocal one-body density in single-particle coordinates, from which we subsequently obtain the translationally-invariant nonlocal one-body density [53] that is used as input to the NA scattering calculation [19].

All three nuclei under consideration here have 0^+ ground states; both ^4He and ^{16}O are closed-shell nuclei, whereas ^{12}C has a deformed ground state. For ^4He and ^{16}O , the most important ground state observables are the energy and the charge radius; while for ^{12}C the quadrupole moment of the first excited state, which is a rotational excitation of the ground state with $J = 2$, also gives information about the deformation. The experimental charge radius is related to the point-proton structure radius via

$$r_{\text{str}}^2 = r_{\text{charge}}^2 - \left(R_p^2 + \frac{N}{Z} R_n^2 + \frac{3}{4m_p^2} \right), \quad (5)$$

with R_p^2 and R_n^2 the proton and neutron mean-square charge radii (note that R_n^2 is negative), and m_p is the proton mass.

Of course, the NCSM calculations depend on the truncation parameter, N_{max} , and the HO parameter, $\hbar\omega$; only in the limit of $N_{\text{max}} \rightarrow \infty$ do the physical observables become independent of $\hbar\omega$. For ^4He , we can perform our numerical calculations at sufficiently large N_{max} so that our wavefunctions are almost converged, but for ^{12}C (see Fig. 3) and ^{16}O we are limited to $N_{\text{max}} = 10$ on current computational resources. This is sufficiently large to perform an extrapolation of the obtained ground state energies to the complete basis, see Table I, but radii, and more general, densities, tend to converge significantly slower, as can be seen in Fig. 3 for ^{12}C ; the $\hbar\omega$ and N_{max} dependence for ^{16}O is similar. We therefore give in Table I our result for the point-proton structure radii at the largest N_{max} over the range $16 \text{ MeV} < \hbar\omega < 24 \text{ MeV}$ ($15 \text{ MeV} < \hbar\omega < 25 \text{ MeV}$ for Daejeon16) which is a compromise of a common range

	${}^4\text{He}$	${}^{12}\text{C}$	${}^{16}\text{O}$
	Ground state energy (MeV)		
Daejeon16	-28.372(1)	-92.9(0.1)	-131.3(0.3)
NNLO _{opt}	-27.596(1)	-88.4(1.3)	-133.(3.)
EKM N2LO	-28.11(1)	-93.8(3.3)	-149.(5.)
expt.	-28.296	-92.16	-127.62
	RMS point-proton structure radius (fm)		
Daejeon16	1.514 ~ 1.513	2.30 ~ 2.27	2.40 ~ 2.32
NNLO _{opt}	1.440 ~ 1.436	2.30 ~ 2.14	2.35 ~ 2.17
EKM N2LO	1.450 ~ 1.416	2.29 ~ 2.05	2.28 ~ 2.05
expt.	1.484(6)	2.341(5)	2.58(1)

TABLE I. Ground state energy (top, extrapolated to the complete basis) and point-proton radius (bottom) obtained with the Daejeon16 potential [35], the NNLO_{opt} [34] chiral potential, and the EKM chiral potential at order N2LO [4, 5], as well as the experimental values.

for all three potentials in which both the energy converges reasonably well and the radius appears to converge. This is also the range in $\hbar\omega$ that we use for our calculations of scattering observables in Sec. IV.

Numerical convergence is significantly better with Daejeon16 than with the other two potentials, as one would expect: although Daejeon16 is based on a chiral EFT potential, like the other two potentials, Daejeon16 is specifically designed to have improved numerical convergence of NCSM calculations by applying an SRG evolution on the initial chiral EFT NN potential [35]. On the other hand, the EKM N2LO potential has the slowest convergence, both for the energies and for the radii.

Table I clearly shows that Daejeon16 also gives the best agreement with the experimental values for these three nuclei – which is not surprising since the ground state energies of these nuclei (as well as several others) were included in the fitting of Daejeon16 [35]. Interestingly, NNLO_{opt} leads to noticeable underbinding of both ${}^4\text{He}$ and ${}^{12}\text{C}$, while all three interactions overbind ${}^{16}\text{O}$, though by different amounts.

The obtained point-proton structure radii are in reasonable agreement with experiment for ${}^4\text{He}$ and slightly too small for ${}^{12}\text{C}$, but significantly too small for ${}^{16}\text{O}$, although it is hard to quantify this discrepancy due to the slow convergence of radii in a HO basis. The structure radii being too small for ${}^{16}\text{O}$ is correlated with the overbinding of ${}^{16}\text{O}$; indeed, the deviation between experiment and calculation in both the ground state energy and the structure radius is largest with the EKM N2LO potential and smallest with Daejeon16.

Although neither the radius of the ${}^{12}\text{C}$ ground state, nor the quadrupole moment of the $J = 2$ rotational excitation, are very well converged, as shown in Ref. [54] for a subset of the same NN interactions, the dimensionless ratio Q/r_{str}^2 is much better converged, and for all three interactions here it is in agreement with the experimental value, given the large experimental uncertainties. The obtained excitation energy is also in reasonable agreement with experiment, to within the estimated uncertainties in our calculations.

Before moving to the scattering applications, it is also illustrative to look at the local densities of these three nuclei, with these three different NN interactions, as well as their charge form factors. In Fig. 4 we show the local point-proton densities, normalized so they integrate to the total number of protons. The colored bands in this and subsequent figures correspond to the same range in the HO parameter as used for the radii listed in Table I, $16 \text{ MeV} < \hbar\omega < 24 \text{ MeV}$ ($15 \text{ MeV} < \hbar\omega < 25 \text{ MeV}$ for Daejeon16), with the dashed and solid lines our results at $\hbar\omega = 20 \text{ MeV}$. We clearly see that the local density is spread out furthest with Daejeon16, whereas the EKM N2LO potential leads to the most compact densities, as is also evident from the differences in the structure radii in Table I; furthermore we see that the numerical convergence is significantly better with Daejeon16 than with the other two potentials, again, as expected.

Finally, we can calculate the electric charge form factor from the Fourier transform of the one-body densities, ignoring contribution from two-body currents. For point-nucleons, the charge form factor would simply be the Fourier transform of the proton density. In order to compare with the experimental form factors however, we do need to incorporate the fact that the protons and neutrons are not point-particles. For the longitudinal form factor we have

$$F(q) = \frac{1}{Z} \frac{G_E^p(Q_{\text{el}}^2) F_p(q) + G_E^n(Q_{\text{el}}^2) F_n(q)}{\sqrt{1 + Q_{\text{el}}^2/(4m_N^2)}}, \quad (6)$$

where $F_{p,n}(q)$ are the Fourier transforms of the local point-proton and -neutron densities, $G_E^{p,n}(Q^2)$ the proton and neutron electric form factors, and $Q_{\text{el}}^2 = q^2 - \omega_{\text{el}}^2$ the four-momentum squared, with $\omega_{\text{el}} = \sqrt{q^2 + m_A^2} - m_A$ the energy transfer corresponding to the elastic peak and m_A the mass of the nucleus. Here we take the parameterization of [55] for the proton and neutron form factors $G_E^{p,n}(Q^2)$. Note that the charge radius in Eq. (5) is related to the form factor

via

$$r_{\text{charge}}^2 = -6 \frac{dF(q^2)}{dq^2} \Big|_{q=0}, \quad (7)$$

and similarly, the proton and neutron radii $R_{p,n}^2$ to the derivatives of $G_E^{p,n}$, and the point-proton structure radius to derivative of F_p ; indeed, Eq. (5) follows directly from Eq. (6) by taking the derivative with respect to q^2 , followed by setting $q = 0$.

In Figs. 5 and 6 we show our results for the charge form factors, compared to experimental data. Interestingly, although the obtained form factors for ${}^4\text{He}$ agrees with experiment at small momenta (as could be expected based on the agreement with experiment for the point-proton structure radius), it disagrees for $q > 2 \text{ fm}^{-1}$, for all three interactions. In particular, the first zero-crossing happens between 4.4 and 4.8 fm^{-1} , whereas the experimental data indicate a zero-crossing at or just above 3 fm^{-1} . It is unclear what the origin is of the significant deviation with experiment starting above about 2.5 fm^{-1} – it could be caused by the lack of 3-body forces, the lack of consistent 2-body currents, or simply an indication that the chiral expansion breaks down for larger momenta. Note that, quantum Monte Carlo calculations, both with a phenomenological potential (AV18 plus UIX 3-body forces) and with local N²LO chiral EFT interactions, including 3-body forces give much better agreement with experiment than our current calculations [56].

In contrast the calculated form factors for ${}^{12}\text{C}$ and ${}^{16}\text{O}$ agree qualitatively with experiment up through the first zero-crossing, with the first zero-crossing at only slightly larger momenta q than experimentally observed; this is likely related to the radii being slightly too small. Furthermore, the relative location of the first zero-crossings in ${}^{12}\text{C}$ and ${}^{16}\text{O}$ does agree with the relative differences in the radii, see Table I. Qualitatively similar results were obtained for ${}^{12}\text{C}$ and ${}^{16}\text{O}$ with quantum Monte Carlo calculations, both with a phenomenological potential (AV18 plus 3-body forces) and with local N²LO chiral EFT interactions, including 3-body forces [57].

We should point out that the first minima in the charge form factors for ${}^{12}\text{C}$ and ${}^{16}\text{O}$ occur at momentum transfers smaller than 2 fm^{-1} , that is, at much smaller momentum transfers than for ${}^4\text{He}$. Thus it is an open question if the failure in describing the charge form factor of ${}^4\text{He}$ results from inherent deficiencies in the high momentum behavior of NCSM one-body densities, or from e.g. the lack of 2-body current operators.

Lastly, note that our numerical convergence is best with Daejeon16, as expected; but more interesting is that with Daejeon16 the magnitude of the form factor drops off (much) more rapidly than with the other potentials, not only for ${}^4\text{He}$, but also for ${}^{12}\text{C}$ and ${}^{16}\text{O}$. This is likely a direct consequence of the SRG evolution, which suppresses the high-momentum components.

IV. PROTON-NUCLEUS SCATTERING OBSERVABLES

In this section we present calculations of observables for elastic scattering from the closed shell nuclei ${}^4\text{He}$ and ${}^{16}\text{O}$ and the open-shell nucleus ${}^{12}\text{C}$ based on the three different NN interactions discussed in Section II. The effective interactions are computed based on Eq. (1), which indicates that the NN interactions are treated on the same footing in the structure as well as reaction part. For the laboratory kinetic energies we choose as lowest energy 65 MeV being at the lower limit where the leading order in the spectator expansion may be considered reliable, around 100 MeV where all interactions still describe the NN Wolfenstein amplitudes reasonably well, and a higher energy, around 160 MeV, where differences in the description of the NN Wolfenstein amplitudes become already quite visible. The choice of the specific projectile energies for each target nucleus is based on the availability of experimental data.

The differential cross sections divided by the Rutherford cross section are shown in Fig. 7 for proton scattering from ${}^4\text{He}$, in Fig. 8 from ${}^{12}\text{C}$, and in Fig. 9 from ${}^{16}\text{O}$. In all figures the lines represent the value for $\hbar\omega=20$ MeV, while the bands indicate the variation in $\hbar\omega$ between 16 and 24 for the NNLO_{opt} and EKM interactions and between 15 and 25 for the Daejeon16 interaction. This dependence on $\hbar\omega$ results from the calculation of the scalar and spin-projected one-body densities entering the NA effective interaction in leading order in the spectator expansion, and should become insignificant when N_{max} is large. This is quite well illustrated by contrasting the calculations of ${}^4\text{He}$, which employ $N_{\text{max}} = 18$ to those of ${}^{12}\text{C}$ and ${}^{16}\text{O}$ for which only $N_{\text{max}} = 10$ is computationally feasible.

The leading order of the multiple scattering expansion is usually considered quite reliable at 100 MeV projectile energy and higher, while when moving towards lower energies corrections may start to play a role [58, 59]. Considering the differential cross sections for all three nuclei for energies around 100 MeV and higher and momentum transfers to about 1.5 fm^{-1} we observe that all calculations over-predict the experimental values, with the calculation based on the NNLO_{opt} interaction being closest to the data. This is especially noteworthy, since the squares of the summed np and pp Wolfenstein amplitudes A shown at similar energies in Fig. 1, which represent the central piece of the NN interaction, under-predict the corresponding NN values represented by the Cd-Bonn values at for NN energies exceeding 100 MeV. As also shown in Fig. 1, at 65 MeV all three NN interactions essentially coincide even for very

low momentum transfers. This leads to very similar differential cross sections at this energy at least for the p -shell nuclei ^{12}C and ^{16}O at the same energy, though here all calculations under-predict the experimental values.

The predictions of the differential cross section for ^4He for the energies shown in Fig. 7 do not describe the experiment beyond about $q \simeq 1 \text{ fm}^{-1}$. This may be related to the charge form factor of ^4He , as calculated with these interactions, being far from experiment in the first minimum as illustrated in Fig. 5; or it could be an indication of e.g. a deficiency of the leading-order spectator expansion for the tightly-bound s -shell nucleus ^4He at energies well below 200 MeV. For both p -shell nuclei, ^{12}C and ^{16}O , the calculated first minimum of the charge form factor is much closer to experiment, albeit at a slightly higher momentum transfer. This results in the maximum-minimum structure within the differential cross sections for those nuclei also being shifted to slightly higher momentum transfers.

Next, we consider spin observables for the same nuclei at the same energies. There are two independent spin observables that can be obtained for scattering of a spin- $\frac{1}{2}$ particle from a spin-0 target, namely the analyzing power A_y and the spin-rotation function Q . The analyzing power considers the projectile spin normal to the scattering plane, while the spin-rotation function refers to the change of the spin direction in the scattering plane. To experimentally determine the latter, a double scattering measurement must be performed, a reason why experimental information for the spin-rotation function is relatively scarce. The analyzing powers for proton scattering from ^4He are shown in Fig. 10, from ^{12}C in Fig. 11, and from ^{16}O in Fig. 12. The error bands represent different values of $\hbar\omega$ in the calculation of the nonlocal one-body densities. The results for ^4He use $N_{\text{max}} = 18$, Fig. 7 shows that those calculations are well converged. This is not the case for ^{12}C and ^{16}O , where $N_{\text{max}} = 10$ is the highest value that can reasonably be used in the structure calculation. Nevertheless, for momentum transfers below 1.5 fm^{-1} all calculations are reasonably converged. For both p -shell nuclei, ^{12}C and ^{16}O , we observe a common behavior as function of energy. At the lowest energy, 65 MeV, the experimental data for the analyzing power are consistent with zero up to about 1 fm^{-1} , and then quickly rise to their maximum value of one. The position of this first maximum is captured by all three calculations reasonably well, while none of them reflects an almost zero analyzing power for very small momentum transfers. For ^4He at 65 MeV, the experimental values of the analyzing power is very small over the entire range of momentum transfers, which is not captured by any of the calculations. At 100 MeV the slow rise of A_y at momentum transfers smaller than 1 fm^{-1} , is captured better by calculations based on the EKM and Daejeon16 calculations, while the first dip is only reproduced by calculations based on the NNLO_{opt} interaction. At the highest energy shown, only the NNLO_{opt} interaction is able to describe the data, especially over the entire range of momentum transfers shown.

To possibly gain some insight into the behavior of the analyzing power and its energy dependence, we need to remember, that the parameterization in terms of Wolfenstein amplitudes of Eq. (4) can also be used to describe NA scattering. The amplitude for the scattering of a spin- $\frac{1}{2}$ particle from a spin-0 particle is simpler than the one given in Eq. (4) and only contains two Wolfenstein amplitudes, namely $A(\mathbf{q}, \mathcal{K}_{NA})_{NA}$ and $iC(\mathbf{q}, \mathcal{K}_{NA})_{NA} (\boldsymbol{\sigma}^{(0)} \cdot \hat{\mathbf{n}})$ [39, 60]. In this case, there are no tensor amplitudes M , G , and H . For the calculation of observables, only the on-shell pieces of the Wolfenstein amplitudes contribute, and the spin observables are given as

$$\begin{aligned} A_y &= \frac{2\Re [A^*(\mathbf{q}, \epsilon)_{NA} C(\mathbf{q}, \epsilon)_{NA}]}{|A(\mathbf{q}, \epsilon)_{NA}|^2 + |C(\mathbf{q}, \epsilon)_{NA}|^2} \\ Q &= \frac{2\Im [A(\mathbf{q}, \epsilon)_{NA} C^*(\mathbf{q}, \epsilon)_{NA}]}{|A(\mathbf{q}, \epsilon)_{NA}|^2 + |C(\mathbf{q}, \epsilon)_{NA}|^2}, \end{aligned} \quad (8)$$

with \mathbf{q} being the momentum transfer. The unpolarized differential cross section is proportional to the denominator in the above expressions. The expressions for A_y as well as Q show that those observables are given by products of real and imaginary parts of the amplitude $A(\mathbf{q}, \epsilon)_{NA}$ representing the central part of the effective NA interaction as well as the spin-orbit part $C(\mathbf{q}, \epsilon)_{NA}$. They also show that they test different combinations of real and imaginary parts of the effective interaction. Having this in mind, it should not be surprising, that a better description of the differential cross section by the NNLO_{opt} interaction leads to a better description of A_y . This is consistent with the findings in Ref. [61], which studied the overlap of parameter spaces when fitting differential cross sections and A_y data based on phenomenological optical potentials in a Bayesian approach. They found that both sets of data ultimately lead to similar likelihood functions and thus similar qualities of their fits. Considering the NN amplitudes for the spin-orbit contribution, Fig. 2, the NNLO_{opt} interaction has for all shown energies a stronger spin-orbit force compared to the other two interactions. This together with a weaker central part seems to lead to a better description of analyzing power for ^{12}C and ^{16}O especially at the higher energies. The prediction of the analyzing power in ^4He is far away from the experimental data. Referring to the observation and discussion of the differential cross section for ^4He , this should not be a surprise. In addition, ^4He is a tightly bound system predominantly in the s -state. The leading order in the spectator expansion may not be sufficient for obtaining the effective NA interaction.

Experimental information for the spin-rotation function Q is considerably sparser compared to the ones for A_y . For proton scattering at 65 MeV data exist for all nuclei we consider here and they are shown in Fig. 13 together with the corresponding calculations. For both, ^{12}C and ^{16}O , the peak and dip structure is captured by all three effective NA interactions almost up to $q \approx 2 \text{ fm}^{-1}$, though the magnitude is not. A study in Ref. [58] for heavier nuclei indicated

that taking into account in an approximate fashion pieces beyond the leading order in the spectator expansion may remedy this situation. The light nucleus ${}^4\text{He}$ again does not fit this scheme at all; here the first dip in the data is not captured by the calculations at all, most likely because of the deficiencies already discussed earlier.

V. EXTRACTION OF THE LOCAL PART OF THE OPTICAL POTENTIALS

As seen in the previous Section, the *ab initio* effective NA interactions derived from three different chiral NN interactions in leading order in the spectator expansion yield differences in NA scattering observables that are comparable or larger to uncertainties that are obtained by chiral effective field theory uncertainties [21, 37]. Though potentials are not observable, they can provide a guide on differences in calculations thereof. Following Eq. (1) the leading order effective NA interaction $\widehat{U}(\mathbf{q}, \mathcal{K}_{NA}, \epsilon)$ is a scalar function of two vector variables, \mathbf{q} and \mathcal{K}_{NA} , and an energy variable ϵ . The two momenta are explicitly given in Eq. (2). Since the potential is considered in the c. m. frame of the projectile-target $(A + 1)$ system, we refer for simplicity to the average momentum here as \mathcal{K} and omit the subscript NA , and also omit the dependence on ϵ . The potential has two pieces, a central and a spin-orbit part, which both are complex functions. To illustrate the functional forms we show in Fig. 14 the central potential $\widehat{U}_C(q, \mathcal{K}, \theta_{q, \mathcal{K}})$ for proton scattering from ${}^{12}\text{C}$ at 65 MeV laboratory kinetic energy obtained *ab initio* from the three different chiral NN interactions we consider. The potentials are shown for the fixed angle $\theta_{q, \mathcal{K}} = 90^\circ$ between the vector variables \mathbf{q} and \mathcal{K} . We verified that potentials depend only weakly on the angle between the two vectors, and thus the potential is almost separable in them as already pointed out in Ref. [25]. This particular property is imprinted on the potential by the nonlocal one-body density, as shown in Ref. [53].

The potential surfaces for $\theta_{q, \mathcal{K}} = 90^\circ$ are special, since for them the on-shell condition

$$q^2 + 4\mathcal{K}^2 = 4k_0^2 \quad (9)$$

is defined. Here k_0 is the on-shell momentum in the NA c. m. frame. The white dashed lines in Fig. 14 indicate this on-shell condition. For this illustration we chose to show the fully-off-shell central part of the effective interaction at 65 MeV, since at this energy the chiral NN amplitudes shown in Fig. 1 given by the interactions are quite similar. However, the interactions lead to different off-shell behavior especially in the variable \mathcal{K} . As pointed out in Sec. II, the Daejeon16 interaction is based on the Idaho N3LO chiral interaction, which is SRG evolved with a flow parameter $\lambda=1.5 \text{ fm}^{-1}$. A characteristic of an SRG evolution is that the interaction becomes softer while its on-shell characteristics is preserved. The effective interaction based on the Daejeon16 interactions falls off fastest as function of the variable \mathcal{K} , while both, the EKM and the NNLO_{opt} interactions exhibit stronger, albeit different off-shell behavior in \mathcal{K} , especially in the real part of $\widehat{U}_C(q, \mathcal{K}, \theta_{q, \mathcal{K}})$.

If we want a more quantitative view of the effective potentials, we should focus on a part which can be connected to a local potential. It was shown in Ref. [25] that the most important piece of the potential contributing in the scattering calculation is the local part of the potential, while the nonlocal part could be approximated with terms of a Gaussian non-locality. This means that the far off-shell differences shown in Fig. 14 likely contribute little to elastic scattering observables. We want to pursue this line of thought further. With the help of the on-shell condition, Eq. (9), we can obtain from the potential surfaces (central as well as spin-orbit) $\widehat{U}(q, \mathcal{K}, \theta_{q, \mathcal{K}} = 90^\circ)$ a function $\widehat{U}(q)$ at a given scattering energy, which we then Fourier transform to obtain functions $\widehat{U}_C(\zeta)$ and $\widehat{U}_{SO}(\zeta)$. The radial variable $\zeta = \frac{1}{2}(r' + r)$ is the conjugate variable to the momentum transfer q [53], if one would consider nonlocal potentials in coordinate space as functions of r and r' . To avoid confusion we refer to the local coordinate as ζ .

When calculating observables we first construct the Watson optical potential according to Eq. (3). Since this procedure is not feasible in coordinate space we apply the well known KMT factor $(A-1)/A$ [62] to obtain local optical potentials $U_C(\zeta)$ and $U_{SO}(\zeta)$. The KMT approximation represents scattering observables obtained from a Watson optical potential very well for momentum transfers up to about 2.5 fm^{-1} [37, 63], and should be applied when comparing scattering calculations with the extracted local potential to calculations based on the non-local Watson optical potential.

The local effective central potentials for proton scattering from ${}^{12}\text{C}$ obtained this way are shown in Fig. 15. First, we observe that all curves exhibit a Woods-Saxon shape, as it should be expected from the central part of local optical potentials. Next, we need to point out that one should not concentrate on differences in the potentials for $\zeta \rightarrow 0$, since the coordinate space Schrödinger equation multiplies a factor ζ^2 to the potential. More important are differences for ζ between 1 and 3 fm. While at 65 MeV the three different potentials are quite similar in this range, at the higher energies there is a striking difference between the potential extracted from NNLO_{opt} compared to the other two for the real central part. The real central optical potential extracted from NNLO_{opt} becomes weaker as the energy increases, which is consistent with the better description of the differential cross sections shown in Fig. 8, and

which can be traced back to a weaker central NN part in NNLO_{opt} as shown in Fig. 1. The imaginary parts of the central optical potential do not exhibit a strong energy dependence.

Obtaining the local part of the spin-orbit potentials in coordinate space is more involved. The momentum space representation of the spin-orbit operator is given by $i(\boldsymbol{\sigma}^{(0)} \cdot \hat{\mathbf{n}})$, where $\hat{\mathbf{n}}$ is a vector normal to the scattering plane, Eq. (2), leading to a sine function in the momentum space \hat{U}_{SO} . To obtain $U_{SO}(\zeta)$ we multiply with the KMT factor and normalize the spin-orbit potential so that it is compatible with standard coordinate space scattering codes [64, 65] that define the spin-orbit potential as $\frac{2}{\zeta}U_{SO}(\zeta)(\mathbf{l} \cdot \boldsymbol{\sigma}^{(0)})$, where \mathbf{l} is the orbital angular momentum and $\boldsymbol{\sigma}^{(0)}$ the spin of the projectile.

The local parts of the spin-orbit potentials based on the three different chiral NN interactions are shown in Fig. 16. The real parts are relatively similar, with the NNLO_{opt} interactions being the strongest. This is consistent with the NN Wolfenstein amplitudes C shown in Fig. 2, where the NNLO_{opt} shows the largest spin-orbit contribution. The imaginary spin-orbit potential is roughly an order of magnitude smaller than the real part. In some phenomenological optical potentials [66] it was also found that the imaginary part is quite small, and was thus omitted. Other phenomenological optical potentials [67] include it, however the fit returns it as being quite small.

The local parts of the effective potentials as shown in Fig. 15 exhibit for both the real and imaginary pieces Woods-Saxon shapes. We picked the potentials based on $\hbar\omega = 20$ MeV and were able to fit them with 3 Woods-Saxon terms. We found that the spin-orbit term can also be very well represented by Woods-Saxon terms multiplied by the radial variable ζ . The details are given in the Appendix. To put this into perspective with calculations of NA scattering observables, we then use the Woods-Saxon parameterization of the local part of the *ab initio* effective interaction obtained from the NNLO_{opt} chiral interaction and calculate scattering observables at 160 MeV using a coordinate space differential equation solver, and compare this result with the full calculation (Fig. 17). This comparison gives insight into the importance of the nonlocal structure of the *ab initio* leading order NA effective interaction. In all the observables, differential cross section and spin observables, the differences are quite small at forward angles, i.e. small momentum transfers. This indicates that at small momentum transfers the nonlocal structure contributes little, since here the scattering can be viewed as a grazing of the nucleus by the projectile. However as the momentum transfer grows the projectile enters the target and non-local effects become important.

VI. CONCLUSIONS

In this work we study structure and elastic scattering observables for light nuclei up the p -shell in an *ab initio* framework for three different NN interactions based on chiral effective field theory. We concentrate on the closed shell nuclei ${}^4\text{He}$ and ${}^{16}\text{O}$, and the open-shell nucleus ${}^{12}\text{C}$. The elastic scattering observables are calculated in leading order in the spectator expansion. This means that two nucleons are active in the scattering process, and no explicit three-nucleon forces are included in the scattering process. Therefore, we concentrate on two chiral interactions up to next-to-next-to-leading (NNLO) order, namely the NNLO_{opt} interaction from Ref. [34], and the EKM interaction from Refs. [4, 5] up to N2LO. The Daejeon16 interaction [35] starts from the Idaho N3LO chiral interaction [49], which is SRG evolved with a flow parameter $\lambda=1.5$ fm $^{-1}$ and cast into a harmonic oscillator basis. The NNLO_{opt} chiral interactions is fitted up to a NN laboratory energy of about 125 MeV, while the other two interactions give a good description of NN to at least 200 MeV. We compare the NN Wolfenstein amplitudes A and C which are relevant for NA scattering from nuclei with a 0^+ ground state to amplitudes calculated from a ‘high-precision’ NN potential that can serve as representing NN data, and see that the NNLO_{opt} interaction provides a weaker central interaction at energies higher than 125 MeV. It also has a slightly stronger spin-orbit force.

When considering structure observables, we focus on those that are dominated by one-body densities. The latter enter the calculation of the leading order term of the spectator expansion, and thus may give a connection between structure and scattering observables. We presented ground state energies and point-proton radii calculated with our choice of NN interactions as well as the corresponding charge form factors. For the p -shell nuclei ${}^{12}\text{C}$ and ${}^{16}\text{O}$ the calculated charge form factors are reasonably close to experiment, though the minima in both cases are located at slightly higher momentum transfers, which should be related to the point-proton structure radius being predicted too small. The calculated charge form factor for ${}^4\text{He}$ is close to experiment up to about a momentum transfer of 2 fm $^{-1}$, but completely misses the dip at about 3 fm $^{-1}$; the origin of this deficiency is unclear but it could be an indication that the chiral expansion breaks down for larger momenta.

The translationally invariant off-shell one-body densities together with the off-shell NN Wolfenstein amplitudes A , C , and M enter the calculations for the leading order effective NA interaction for proton-nucleus elastic scattering observables are derived. For the p -shell nuclei ${}^{12}\text{C}$ and ${}^{16}\text{O}$ we find that at the lowest projectile energy we consider, 65 MeV, all three chiral NN interactions give relatively similar descriptions of the differential cross sections and under-predict the first maximum, while at both higher energies, 100 MeV and 160 (180) MeV, they over-predict the experiment. The NNLO_{opt} is closest to the experiment, though under-predicting the NN Wolfenstein amplitudes.

In order to gain insight into this apparent contradiction, we extracted the local part of the effective NA interaction and found that indeed the real part of the central potential calculated from the NNLO_{opt} interaction is considerable weaker than those extracted from the other interactions for energies higher than 100 MeV. The extracted imaginary parts of the central potential are relatively similar as function of energy for the three chiral NN interactions.

Since the spin observables are calculated as products of real and imaginary parts of NA Wolfenstein amplitudes the large difference in the real central part between the NNLO_{opt} interaction and the EKM and Daejeon16 interaction propagates to the description of the analyzing power for ^{12}C and ^{16}O . Here only the calculations based on the NNLO_{opt} chiral interaction reproduce the shape of A_y for energies larger than 100 MeV.

The situation is slightly different for ^4He , where for all energies considered the differential cross section is overpredicted by the calculations when considering momentum transfers up to about $1.5\text{-}2.0\text{ fm}^{-1}$, i.e. for the first maximum in the cross section. This momentum range is similar to the one for which the calculated charge form factor matches the corresponding data. Therefore, one can not point to a single reason why the proton differential cross section is not well described at higher momentum transfers. Though again the NNLO_{opt} chiral interaction gives the best description from the three interactions. The analyzing powers shown at the same energies are not well described either, although earlier work [19] showed a very good description of differential cross section and analyzing power based on the NNLO_{opt} chiral interaction at 200 MeV projectile energy. For the tightly bound s -wave dominated nucleus ^4He it may very be the case that higher orders in the spectator expansion are important for a better description of the lower energy observables.

Summarizing, our studies show that our choice of three NN interactions that are based on a chiral field theory framework and calibrated to reproduce similar data in the few-nucleon sector predict NA scattering observables quite differently. Going into more detail by considering the calculated effective NA interactions and extracting their local parts may be able to point to pieces in the NN interactions that dominate their performance in NA calculations.

ACKNOWLEDGMENTS

This work was performed in part under the auspices of the U.S. Department of Energy under contract Nos. DE-FG02-93ER40756 and DE-SC0023495. The numerical computations benefited from computing resources provided by the National Energy Research Scientific Computing Center (NERSC), a U. S. DOE Office of Science User Facility located at Lawrence Berkeley National Laboratory, operated under contract No. DE-AC02-05CH11231.

Appendix A: Woods-Saxon parameterization of the local parts of the effective NA interactions for ^{12}C

The parameterization of local optical potentials in terms of Woods-Saxon shapes has a long history. Specifically, code packages like FRESKO [65, 68] and ECIS [69, 70] allow to enter parameters based on Woods-Saxon parameterization to be entered for calculating elastic NA scattering observables. In order to investigate if the local parts of the effective interactions for ^{12}C we calculated *ab initio* follow standard expectations of having Woods-Saxon shapes, we list the coefficients for a local coordinate space parts of the optical potentials for ^{12}C featured in this work at three different proton projectile energies. We choose the calculations based on $\hbar\omega = 20$ MeV and $N_{\text{max}} = 10$ from Figs. 15 and 16. We find that three Woods-Saxon shapes are sufficient in all cases to represent the local parts of the effective interaction, when setting as criteria that the analytical function correlate with the numerical results at high precision (> 0.9999). Figure 17 of the main text shows as dashed line a scattering calculation which featuring the NNLO_{opt} chiral potential from Ref. [34] with a proton projectile at 160 MeV. The dashed-dotted line is calculated using the optical potential based on the coefficients listed in this appendix which are processed through an ECIS type r-space scattering code.

1. Parameters for the central part of the extracted local optical potential

The central part of the optical potentials is described by three Woods-Saxon terms for the real and imaginary part:

$$\begin{aligned}\Re U_c(\zeta) &= \sum_{i=1}^3 V_i \frac{1}{1 + e^{\left(\frac{\zeta - R_i}{a_i}\right)}} \\ \Im U_c(\zeta) &= \sum_{i=1}^3 W_i \frac{1}{1 + e^{\left(\frac{\zeta - S_i}{b_i}\right)}}\end{aligned}\quad (\text{A1})$$

Three different energies are fitted separately, all the central potentials form the traditional negative energy nuclear well.

TABLE II. Woods-Saxon parameters for $\Re U_c(\zeta)$ for ^{12}C based on the NNLO_{opt} [34] chiral NN potential at the energies indicated.

	65 MeV	122 MeV	160 MeV
V_1	-2.9585	-9.0907	-7.4562
V_2	-35.8338	-11.6254	-3.8378
V_3	10.3808	3.8241	1.5649
R_1	4.1455	3.3838	3.4214
R_2	2.0327	1.6355	1.2032
R_3	0.7625	0.6023	2.4738
a_1	0.3194	0.5202	0.5283
a_2	0.5487	0.4387	0.3217
a_3	0.3402	0.2591	0.3207

TABLE III. Woods-Saxon parameters for $\Re U_c(\zeta)$ for ^{12}C based on the EKM [4, 5] chiral NN potential up to N2LO at the energies indicated.

	65 MeV	122 MeV	160 MeV
V_1	-1.2962	-16.6887	-16.8768
V_2	-49.5527	-15.5814	-14.8252
V_3	9.4976	-6.3532	-5.6641
R_1	4.1469	2.9288	2.9069
R_2	1.9121	1.8347	1.6688
R_3	0.6190	1.1140	0.8959
a_1	0.2593	0.5773	0.5825
a_2	0.6276	0.4057	0.4322
a_3	0.4956	0.2870	0.2696

TABLE IV. Woods-Saxon parameters for $\Re U_c(\zeta)$ for ^{12}C based on the Daejeon16 [35] NN potential at the energies indicated.

	65 MeV	122 MeV	160 MeV
V_1	-3.2707	-19.1730	-14.9108
V_2	-37.4844	-10.4265	-9.8969
V_3	4.6176	-3.5101	-4.9593
R_1	3.8250	2.7855	2.9483
R_2	2.0646	1.6311	1.4607
R_3	0.5782	0.8474	0.7528
a_1	0.9023	0.6543	0.6082
a_2	0.5911	0.4200	0.4283
a_3	0.3803	0.2468	0.2413

TABLE V. Woods-Saxon parameters for $\Im m U_c(\zeta)$ for ^{12}C based on the NNLO_{opt} NN potential at the energies indicated.

	65 MeV	122 MeV	160 MeV
W_1	-19.3663	-14.2327	-13.7046
W_2	-22.2666	-15.3673	-14.3915
W_3	-6.0634	-6.6642	-6.5563
S_1	1.5788	1.4190	1.4850
S_2	2.5801	2.7300	2.7570
S_3	0.8166	0.7380	0.7570
b_1	0.4035	0.4105	0.4262
b_2	0.5590	0.5645	0.5462
b_3	0.2433	0.2346	0.2436

TABLE VI. Woods-Saxon parameters for $\Im m U_c(\zeta)$ for ^{12}C based on the EKM NN potential at the energies indicated.

	65 MeV	122 MeV	160 MeV
W_1	-15.7595	-12.6308	-11.0227
W_2	-28.7883	-15.6105	-13.1028
W_3	-4.7952	-4.8887	-4.7258
S_1	1.5426	1.5055	1.5297
S_2	2.3406	2.6002	2.6623
S_3	0.8233	0.7712	0.7698
b_1	0.3747	0.4097	0.4253
b_2	0.5709	0.5727	0.5625
b_3	0.2270	0.2376	0.2436

TABLE VII. Woods-Saxon parameters for $\Im m U_c(\zeta)$ for ^{12}C based on the Daejeon16 NN potential at the energies indicated.

	65 MeV	122 MeV	160 MeV
W_1	-21.5698	-11.6742	-11.2472
W_2	-17.7607	-11.0697	-7.9812
W_3	-7.4589	-4.7278	-4.7165
S_1	1.6083	1.5843	1.6829
S_2	2.8052	2.8878	3.0711
S_3	0.8177	0.8136	0.8578
b_1	0.4242	0.4419	0.4714
b_2	0.5218	0.5893	0.5571
b_3	0.2544	0.2561	0.2748

TABLE VIII. Woods-Saxon parameters for $\Re U_{SO}(\zeta)$ for ^{12}C based on the NNLO_{opt} NN potential at the energies indicated.

	65 MeV	122 MeV	160 MeV
V _{so1}	-3.2704	-1.8966	-2.3383
V _{so2}	-0.2579	-0.7528	0.0
R _{so1}	2.1307	2.3350	2.0813
R _{so2}	1.5961	1.7201	
aso ₁	0.4663	0.4610	0.4946
aso ₂	0.2043	0.2681	

TABLE IX. Woods-Saxon parameters for $\Re U_{SO}(\zeta)$ for ^{12}C based on the EKM NN potential at the energies indicated.

	65 MeV	122 MeV	160 MeV
V _{so1}	-1.7713	-2.3492	-1.8878
V _{so2}	-1.6051	0.0	0.0
R _{so1}	2.2809	1.9516	1.9512
R _{so2}	1.5784		
aso ₁	0.4889	0.5267	0.5275
aso ₂	0.4493		

2. Parameters for the spin-orbit part of the extracted local optical potential

For the Spin-Orbit potential, the following functional forms were most appropriate for our data:

$$\begin{aligned}\Re U_{SO}(\zeta) &= \sum_i V_{so_i} \frac{\zeta}{1 + e^{\left(\frac{\zeta - R_{so_i}}{a_{so_i}}\right)}} \\ \Im U_{SO}(\zeta) &= \sum_i W_{so_i} \frac{\zeta}{1 + e^{\left(\frac{\zeta - S_{so_i}}{b_{so_i}}\right)}}\end{aligned}\quad (\text{A2})$$

Here we varied the amount of Woods-Saxon terms needed, our objective again was to obtaining an excellent correlation (> 0.9999). Since many r-space codes (like FRESKO [64, 65, 68] for example) add an obligatory $\frac{2}{\zeta}$ to their spin orbit term. The complete term run through the r-space scattering code is

$$\mathcal{U}_{SO} = \frac{2}{\zeta} U_{SO}(\zeta) (2\vec{l} \cdot \vec{\sigma}), \quad (\text{A3})$$

where our contribution, $U_{SO}(\zeta)$, is defined in Eq. A2. The second factor of 2, included with the vector operator, is tradition within most r-space scattering codes. We found in all the cases listed here that the real spin-orbit formed a large attractive nuclear well while the imaginary term formed a smaller repulsive well. These results are in line with most phenomenological results.

TABLE X. Woods-Saxon parameters for $\Re U_{SO}(\zeta)$ for ^{12}C based on the Daejeon16 NN potential at the energies indicated.

	65 MeV	122 MeV	160 MeV
V _{so1}	-2.4902	-1.6768	-1.4797
V _{so2}	-1.5978	-0.6924	-0.4470
V _{so3}	0.1368	0.03618	0.0
R _{so1}	2.3504	2.3691	1.9384
R _{so2}	1.5573	1.6801	2.9354
R _{so3}	4.8284	4.7296	
aso ₁	0.5137	0.5229	0.4377
aso ₂	0.4405	0.3417	0.4365
aso ₃	0.5732	0.6223	

TABLE XI. Woods-Saxon parameters for $\Im m U_{SO}(\zeta)$ for ^{12}C based on the NNLO_{opt} NN potential at the energies indicated.

	65 MeV	122 MeV	160 MeV
$W_{\text{so}1}$	0.4369	0.4194	0.7072
$W_{\text{so}2}$	-0.2054	0.1387	0.0
$S_{\text{so}1}$	2.6510	1.9424	2.013
$S_{\text{so}2}$	0.9638	3.1285	
$b_{\text{so}1}$	0.6273	0.5067	0.5988
$b_{\text{so}2}$	0.3738	0.5462	

TABLE XII. Woods-Saxon parameters for $\Im m U_{SO}(\zeta)$ for ^{12}C based on the EKM NN potential at the energies indicated.

	65 MeV	122 MeV	160 MeV
$W_{\text{so}1}$	0.8261	0.3767	0.3843
$W_{\text{so}2}$	-0.5784	0.0	0.0
$S_{\text{so}1}$	2.3345	2.3452	2.1325
$S_{\text{so}2}$	1.6682		
$b_{\text{so}1}$	0.6391	0.6396	0.6540
$b_{\text{so}2}$	0.6645		

TABLE XIII. Woods-Saxon parameters for $\Im m U_{SO}(\zeta)$ for ^{12}C based on the Daejeon16 NN potential at the energies indicated.

	65 MeV	122 MeV	160 MeV
$W_{\text{so}1}$	0.3018	0.1932	0.1664
$W_{\text{so}2}$	-0.4981	-0.1558	-0.0609
$S_{\text{so}1}$	2.8836	2.9440	2.9051
$S_{\text{so}2}$	1.0721	0.9685	0.9725
$b_{\text{so}1}$	0.6643	0.6404	0.6048
$b_{\text{so}2}$	0.4454	0.3715	0.2847

-
- [1] D. R. Entem and R. Machleidt, *Phys. Rev. C* **68**, 041001 (2003).
- [2] E. Epelbaum, *Prog. Part. Nucl. Phys.* **57**, 654 (2006).
- [3] E. Epelbaum, H.-W. Hammer, and U.-G. Meißner, *Rev. Mod. Phys.* **81**, 1773 (2009), arXiv:0811.1338 [nucl-th].
- [4] E. Epelbaum, H. Krebs, and U. G. Meißner, *Phys. Rev. Lett.* **115**, 122301 (2015), arXiv:1412.4623 [nucl-th].
- [5] E. Epelbaum, H. Krebs, and U. G. Meißner, *Eur. Phys. J. A* **51**, 53 (2015), arXiv:1412.0142 [nucl-th].
- [6] P. Reinert, H. Krebs, and E. Epelbaum, *Eur. Phys. J. A* **54**, 86 (2018), arXiv:1711.08821 [nucl-th].
- [7] R. Machleidt and D. R. Entem, *Phys. Rept.* **503**, 1 (2011), arXiv:1105.2919 [nucl-th].
- [8] D. R. Entem, R. Machleidt, and Y. Nosyk, *Phys. Rev. C* **96**, 024004 (2017), arXiv:1703.05454 [nucl-th].
- [9] D. Langr, T. Dytrych, J. P. Draayer, K. D. Launey, and P. Tvrđik, *Comp. Phys. Comm.* **244**, 442 (2019).
- [10] D. Langr, T. Dytrych, K. D. Launey, and J. P. Draayer, *The Int. J. of High Performance Computing Applications* **33**, 522 (2019).
- [11] M. Shao, H. M. Aktulga, C. Yang, E. G. Ng, P. Maris, and J. P. Vary, *Comp. Phys. Comm.* **222**, 1 (2018), arXiv:1609.01689 [nucl-th].
- [12] H. M. Aktulga, C. Yang, E. G. Ng, P. Maris, and J. P. Vary, *Concurrency and Computation: Practice and Experience* **26**, 2631 (2014).
- [13] M. Jung, E. H. Wilson, III, W. Choi, J. Shalf, H. M. Aktulga, C. Yang, E. Saule, U. V. Catalyurek, and M. Kandemir, in *Proceedings of the International Conference on High Performance Computing, Networking, Storage and Analysis, SC '13* (ACM, New York, NY, USA, 2013) pp. 75:1–75:11.
- [14] P. Navrátil, J. P. Vary, and B. R. Barrett, *Phys. Rev. Lett.* **84**, 5728 (2000), arXiv:nucl-th/0004058 [nucl-th].
- [15] R. Roth and P. Navrátil, *Phys. Rev. Lett.* **99**, 092501 (2007), arXiv:0705.4069 [nucl-th].
- [16] B. R. Barrett, P. Navrátil, and J. P. Vary, *Prog. Part. Nucl. Phys.* **69**, 131 (2013).
- [17] S. Binder, A. Calci, E. Epelbaum, R. J. Furnstahl, J. Golak, K. Hebeler, T. Hüther, H. Kamada, H. Krebs, P. Maris, Ulf-G. Meißner, A. Nogga, R. Roth, R. Skibiński, K. Topolnicki, J. P. Vary, K. Vobig, and H. Witala (LENPIC Collaboration), *Phys. Rev. C* **98**, 014002 (2018), arXiv:1802.08584 [nucl-th].
- [18] M. Burrows, Ch. Elster, S. P. Weppner, K. D. Launey, P. Maris, A. Nogga, and G. Popa, *Phys. Rev. C* **99**, 044603 (2019), arXiv:1810.06442 [nucl-th].
- [19] M. Burrows, R. B. Baker, Ch. Elster, S. P. Weppner, K. D. Launey, P. Maris, and G. Popa, *Phys. Rev. C* **102**, 034606 (2020), arXiv:2005.00111 [nucl-th].
- [20] R. B. Baker, M. Burrows, Ch. Elster, K. D. Launey, P. Maris, G. Popa, and S. P. Weppner, *Phys. Rev. C* **103**, 054314 (2021), arXiv:2102.01025 [nucl-th].
- [21] R. B. Baker, B. McClung, C. Elster, P. Maris, S. P. Weppner, M. Burrows, and G. Popa, *Phys. Rev. C* **106**, 064605 (2022), arXiv:2112.02442 [nucl-th].
- [22] M. Gennari, M. Vorabbi, A. Calci, and P. Navrátil, *Phys. Rev.* **C97**, 034619 (2018), arXiv:1712.02879 [nucl-th].
- [23] M. Vorabbi, M. Gennari, P. Finelli, C. Giusti, P. Navrátil, and R. Machleidt, *Phys. Rev. C* **105**, 014621 (2022), arXiv:2110.05455 [nucl-th].
- [24] M. Vorabbi, M. Gennari, P. Finelli, C. Giusti, P. Navrátil, and R. Machleidt, *Phys. Rev. C* **103**, 024604 (2021), arXiv:2010.04792 [nucl-th].
- [25] H. F. Arellano and G. Blanchon, *Eur. Phys. J. A* **58**, 119 (2022), arXiv:2206.09461 [nucl-th].
- [26] E. R. Siciliano and R. M. Thaler, *Phys. Rev.* **C16**, 1322 (1977).
- [27] D. J. Ernst, J. T. Londergan, G. A. Miller, and R. M. Thaler, *Phys. Rev.* **C16**, 537 (1977).
- [28] P. C. Tandy and R. M. Thaler, *Phys. Rev.* **C22**, 2321 (1980).
- [29] R. J. Furnstahl, N. Klco, D. R. Phillips, and S. Wesolowski, *Phys. Rev. C* **92**, 024005 (2015), arXiv:1506.01343 [nucl-th].
- [30] J. A. Melendez, S. Wesolowski, and R. J. Furnstahl, *Phys. Rev. C* **96**, 024003 (2017), arXiv:1704.03308 [nucl-th].
- [31] J. A. Melendez, R. J. Furnstahl, D. R. Phillips, M. T. Pratola, and S. Wesolowski, *Phys. Rev. C* **100**, 044001 (2019), arXiv:1904.10581 [nucl-th].
- [32] E. Epelbaum, J. Golak, K. Hebeler, H. Kamada, H. Krebs, Ulf-G. Meißner, A. Nogga, P. Reinert, R. Skibiński, K. Topolnicki, Y. Volkotrub, and H. Witala, *Eur. Phys. J. A* **56**, 92 (2020), arXiv:1907.03608 [nucl-th].
- [33] P. Maris, E. Epelbaum, R. J. Furnstahl, J. Golak, K. Hebeler, T. Hüther, H. Kamada, H. Krebs, Ulf-G. Meißner, J. A. Melendez, A. Nogga, P. Reinert, R. Roth, R. Skibiński, V. Soloviov, K. Topolnicki, J. P. Vary, Yu. Volkotrub, H. Witala, and T. Wolfgruber, *Phys. Rev. C* **103**, 054001 (2021), arXiv:2012.12396 [nucl-th].
- [34] A. Ekström, G. Baardsen, C. Forssén, G. Hagen, M. Hjorth-Jensen, G. R. Jansen, R. Machleidt, W. Nazarewicz, et al., *Phys. Rev. Lett.* **110**, 192502 (2013).
- [35] A. M. Shirokov, I. J. Shin, Y. Kim, M. Sosonkina, P. Maris, and J. P. Vary, *Phys. Lett. B* **761**, 87 (2016), arXiv:1605.00413 [nucl-th].
- [36] A. Picklesimer, P. Tandy, and R. Thaler, *Annals of Physics* **145**, 207 (1983).
- [37] R. B. Baker, M. Burrows, C. Elster, K. D. Launey, P. Maris, G. Popa, and S. P. Weppner, *Front. Phys.* **10**, 1071971 (2023), arXiv:2301.04293 [nucl-th].
- [38] C. Møller, K. Dan. *Vidensk. Sels. Mat. Fys. Medd.* **23**, 1 (1945).
- [39] L. Rodberg and R. Thaler, *Introduction of the Quantum Theory of Scattering*, Pure and Applied Physics, Vol 26 (Academic Press, 1967).
- [40] L. Wolfenstein and J. Ashkin, *Phys. Rev.* **85**, 947 (1952).

- [41] I. Fachruddin, Ch. Elster, and W. Glöckle, *Phys. Rev. C* **62**, 044002 (2000), arXiv:nucl-th/0004057 [nucl-th].
- [42] J. Golak, W. Glöckle, R. Skibinski, H. Witala, D. Rozpedzik, K. Topolnicki, I. Fachruddin, Ch. Elster, and A. Nogga, *Phys. Rev. C* **81**, 034006 (2010), arXiv:1001.1264 [nucl-th].
- [43] Ch. Elster, S. P. Weppner, and C. R. Chinn, *Phys. Rev. C* **56**, 2080 (1997).
- [44] Ch. Elster, T. Cheon, E. F. Redish, and P. C. Tandy, *Phys. Rev. C* **41**, 814 (1990).
- [45] H. F. Arellano and G. Blanchon, *Phys. Rev. C* **98**, 054616 (2018), arXiv:1807.00733 [nucl-th].
- [46] M. Burrows, *Ab Initio Leading Order Effective Interactions for Scattering of Nucleons from Light Nuclei*, Ph.D. thesis, Ohio University (2020).
- [47] J. Henderson et al., *Phys. Lett.* **B782**, 468 (2018), arXiv:1709.03948 [nucl-ex].
- [48] K. D. Launey, A. Mercenne, G. H. Sargsyan, H. Shows, R. B. Baker, M. E. Miora, T. Dytrych, and J. P. Draayer, in *Proceedings of the 4th International Workshop on “State of the Art in Nuclear Cluster Physics” (SOTANCP4)*, Texas (AIP Conf. Proc., 2018).
- [49] D. R. Entem and R. Machleidt, *Phys. Rev.* **C68**, 041001 (2003).
- [50] R. Machleidt, *Phys. Rev. C* **63**, 024001 (2001), arXiv:nucl-th/0006014 [nucl-th].
- [51] H. J. Lipkin, *Phys. Rev.* **110**, 1395 (1958).
- [52] D. H. Gloeckner and R. D. Lawson, *Phys. Lett.* **B53**, 313 (1974).
- [53] M. Burrows, Ch. Elster, G. Popa, K. D. Launey, A. Nogga, and P. Maris, *Phys. Rev. C* **97**, 024325 (2018), arXiv:1711.07080 [nucl-th].
- [54] M. A. Caprio, P. J. Fasano, and P. Maris, *Phys. Rev. C* **105**, L061302 (2022), arXiv:2206.09307 [nucl-th].
- [55] J. J. Kelly, *Phys. Rev. C* **70**, 068202 (2004).
- [56] J. E. Lynn, I. Tews, J. Carlson, S. Gandolfi, A. Gezerlis, K. E. Schmidt, and A. Schwenk, *Phys. Rev. C* **96**, 054007 (2017), arXiv:1706.07668 [nucl-th].
- [57] D. Lonardoni, S. Gandolfi, J. E. Lynn, C. Petrie, J. Carlson, K. E. Schmidt, and A. Schwenk, *Phys. Rev. C* **97**, 044318 (2018), arXiv:1802.08932 [nucl-th].
- [58] C. R. Chinn, C. Elster, R. M. Thaler, and S. P. Weppner, *Phys. Rev. C* **51**, 1418 (1995).
- [59] C. R. Chinn, C. Elster, R. M. Thaler, and S. P. Weppner, *Phys. Rev.* **C52**, 1992 (1995).
- [60] R. Landau, *Quantum Mechanics II, A Second Course in Quantum Theory* (John Wiley and Sons, Inc., 1995).
- [61] M. Catacora-Rios, G. B. King, A. E. Lovell, and F. M. Nunes, *Phys. Rev. C* **104**, 064611 (2021), arXiv:2012.06653 [nucl-th].
- [62] A. K. Kerman, H. McManus, and R. M. Thaler, *Ann. Phys.* **8**, 551 (1959).
- [63] C. R. Chinn, Ch. Elster, and R. M. Thaler, *Phys. Rev. C* **47**, 2242 (1993).
- [64] I. J. Thompson and F. M. Nunes, *Nuclear Reactions for Astrophysics* (Cambridge University Press, 2009).
- [65] I. J. Thompson, *Comput.Phys.Rept.* **7**, 167 (1988).
- [66] R. Varner, W. Thompson, T. McAbee, E. Ludwig, and T. Clegg, *Phys.Rept.* **201**, 57 (1991).
- [67] S. Weppner, R. Penney, G. Diffendale, and G. Vittorini, *Phys.Rev.* **C80**, 034608 (2009).
- [68] I. J. Thompson, “FRESCO reaction code,” <http://www.fresco.org.uk> (1998), version 3.4.
- [69] J. Raynal, “Coupled channel calculations and computer code ECIS,” CEA-CONF-9461 (1988).
- [70] J. Raynal, “ECIS-12: Coupled channel, statistical model, schrodinger and dirac equation, dispersion relation,” <https://rsicc.ornl.gov/codes/psr/psr6/psr-612.html> (2015), available at Oakridge Repository.
- [71] R. F. Frosch, J. S. McCarthy, R. e. Rand, and M. R. Yearian, *Phys. Rev.* **160**, 874 (1967).
- [72] J. S. Mccarthy, I. Sick, and R. R. Whitney, *Phys. Rev. C* **15**, 1396 (1977).
- [73] R. G. Arnold et al., *Phys. Rev. Lett.* **40**, 1429 (1978).
- [74] C. R. Ottermann, G. Kobschall, K. Maurer, K. Rohrich, C. Schmitt, and V. H. Walther, *Nucl. Phys. A* **436**, 688 (1985).
- [75] I. Sick, (unpublished).
- [76] D. Lonardoni, private communication (2023).
- [77] W. Schütz, *Zeitschrift für Physik A Atoms and Nuclei* **273**, 69 (1975).
- [78] I. Sick and J. S. Mccarthy, *Nucl. Phys. A* **150**, 631 (1970).
- [79] K. Imai, K. Hatanaka, H. Shimizu, N. Tamura, K. Egawa, K. Nisimura, T. Saito, H. Sato, and Y. Wakuta, *Nuclear Physics A* **325**, 397 (1979).
- [80] N. P. Goldstein, A. Held, and D. G. Stairs, *Canadian Journal of Physics* **48**, 2629 (1970), <https://doi.org/10.1139/p70-326>.
- [81] V. Comparat, R. Frascaria, N. Fujiwara, N. Marty, M. Morlet, P. G. Roos, and A. Willis, *Phys. Rev.* **C12**, 251 (1975).
- [82] M. Ieiri, H. Sakaguchi, M. Nakamura, H. Sakamoto, H. Ogawa, M. Yosol, T. . Ichihara, N. Isshiki, Y. Takeuchi, H. Togawa, T. Tsutsumi, S. Hirata, T. N. and S. Kobayashi, T. Noro, and H. Ikegami, *Nuclear Instruments and Methods in Physics Research Section A: Accelerators, Spectrometers, Detectors and Associated Equipment* **257**, 253 (1987).
- [83] S. Kato, K. Okada, M. Kondo, K. Hosono, T. Saito, N. Matsuoka, K. Hatanaka, T. Noro, S. Nagamachi, H. Shimizu, K. Ogino, Y. Kadota, S. Matsuki, and M. Wakai, *Phys. Rev. C* **31**, 1616 (1985).
- [84] H. O. Meyer, P. Schwandt, W. W. Jacobs, and J. R. Hall, *Phys. Rev. C* **27**, 459 (1983).
- [85] H. Sakaguchi, M. Nakamura, K. Hatanaka, A. Goto, T. Noro, F. Ohtani, H. Sakamoto, and S. Kobayashi, *Phys. Lett. B* **89**, 40 (1979).
- [86] H. Seifert, *Energy Dependence of the Effective Interaction for Nucleon-Nucleus Scattering*, Ph.D. thesis, University of Maryland (1990).
- [87] J. J. Kelly, J. M. Finn, W. Bertozzi, T. N. Buti, F. W. Hersman, C. Hyde-Wright, M. V. Hynes, M. A. Kovash, B. Murdock, P. Ulmer, A. D. Bacher, G. T. Emery, C. C. Foster, W. P. Jones, D. W. Miller, and B. L. Berman, *Phys. Rev. C* **41**, 2504 (1990).

- [88] J. Wesick, P. Roos, N. Chant, C. Chang, A. Nadasen, *et al.*, *Phys.Rev.* **C32**, 1474 (1985).
- [89] M. Ieiri, H. Sakaguchi, M. Nakamura, H. Sakamoto, H. Ogawa, M. Yosol, T. Ichihara, N. Isshiki, Y. Takeuchi, H. Togawa, T. Tsutsumi, S. Hirata, T. Nakano, S. Kobayashi, T. Noro, and H. Ikegami, *Nucl. Instrum. Methods Phys. Res. A* **257**, 253 (1987).
- [90] M. N. Sakaguchi, H.; Yosoi, *Journal of the Physical Society of Japan* **55(suppl.)**, 61 (1986).

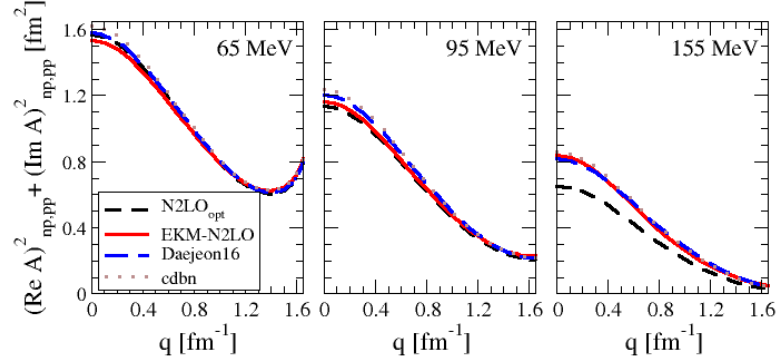


FIG. 1. The sum of the squares of the real and imaginary part of the Wolfenstein amplitude A for pp and np scattering as function of the momentum transfer q at laboratory energies 65, 95, and 155 MeV calculated from the NNLO_{opt} [34] chiral potential (short-dashed), the EKM chiral potential at order N2LO [4, 5] (solid), and the Daejeon16 potential [35] (dashed). As guide to the eye the dotted line represents the same quantity calculated from the Cd-Bonn [50] high precision NN potential.

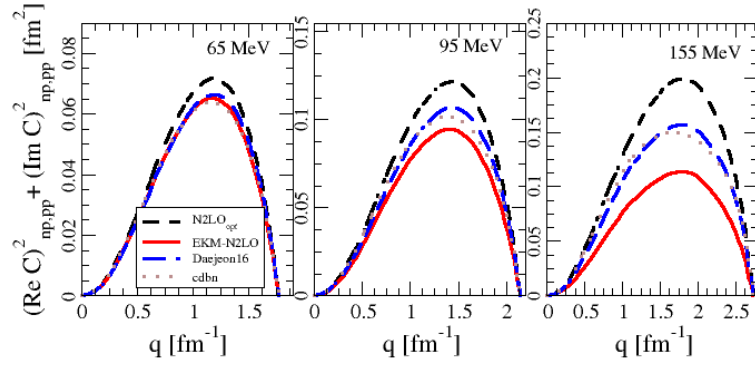


FIG. 2. The sum of the squares of the real and imaginary part of the Wolfenstein amplitude C for pp and np scattering as function of the momentum transfer q at laboratory energies 65, 95, and 155 MeV calculated from the NNLO_{opt} [34] chiral potential (short-dashed), the EKM chiral potential at order N2LO [4, 5] (solid), and the Daejeon16 potential [35] (dashed). As guide to the eye the dotted line represents the same quantity calculated from the Cd-Bonn [50] high precision NN potential.

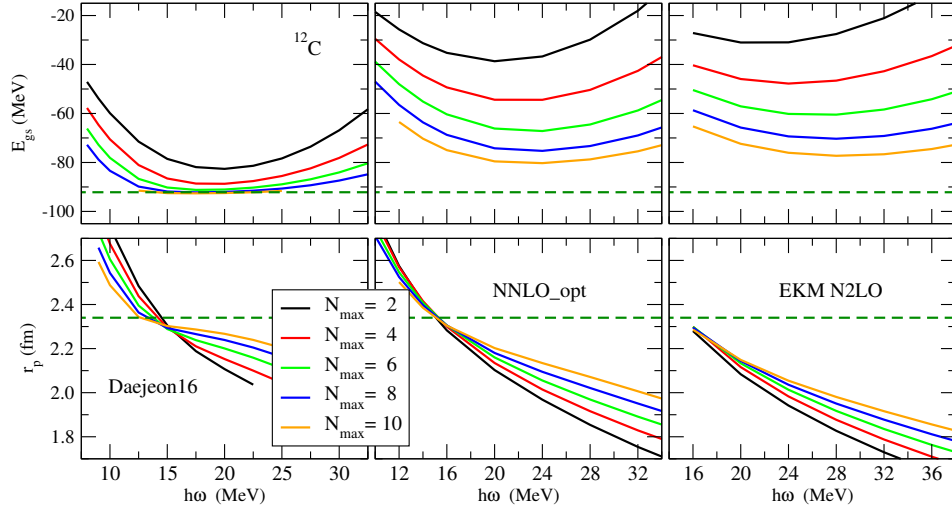


FIG. 3. Ground state energy (top) and point-proton radius (bottom) of ^{12}C obtained with the Daejeon16 potential [35] (left), the NNLO_{opt} [34] chiral potential (center), and the EKM chiral potential at order N2LO [4, 5] (right). The dashed horizontal lines are the experimental values.

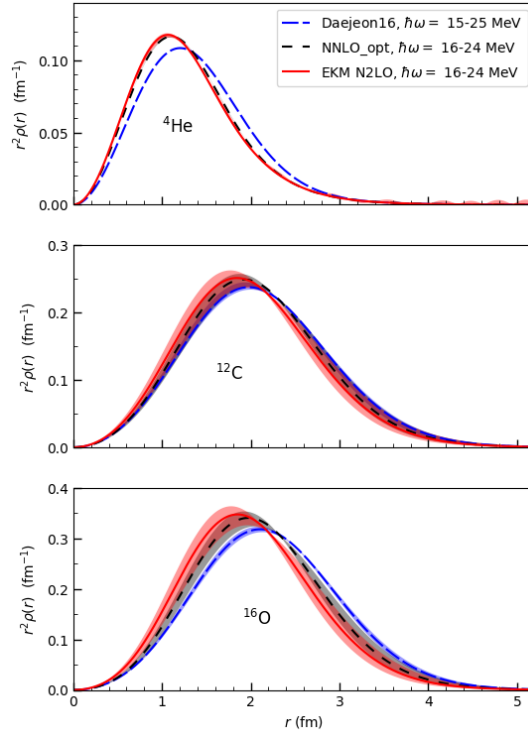


FIG. 4. The local proton density, multiplied by r^2 , of ^4He (top), ^{12}C (middle), and ^{16}O (bottom), obtained with the NNLO_{opt} [34] chiral potential (short-dashed), the EKM chiral potential at order N2LO [4, 5] (solid), and the Daejeon16 potential [35] (dashed). The calculations for ^4He are done at $N_{max} = 18$, those for ^{12}C and ^{16}O at $N_{max} = 10$, all with $\hbar\omega = 20$ MeV. The variation of $\hbar\omega$ from 16 MeV to 24 MeV for the NNLO_{opt} and EKM potentials, and from 15 MeV to 25 MeV for Daejeon16, are indicated by the shaded bands.

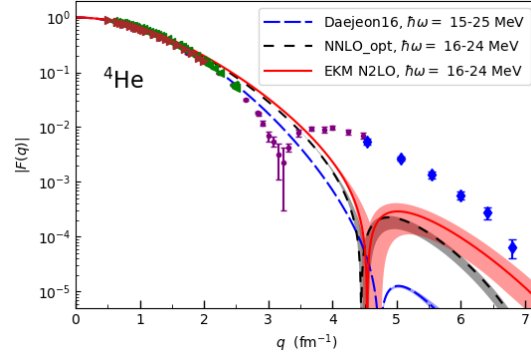


FIG. 5. The calculated charge form factor of ${}^4\text{He}$, with experimental data from Refs. [71–74]. Colors, symbols, and calculational details are the same as in Fig. 4.

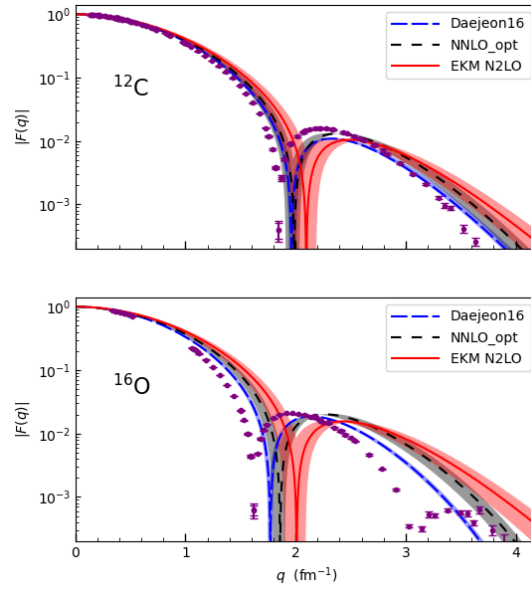


FIG. 6. The charge form factor of ${}^{12}\text{C}$ (top) and ${}^{16}\text{O}$ (bottom), with a compilation of experimental data [75, 76] based on Refs. [77, 78]. Colors, symbols, and calculational details are the same as in Fig. 4.

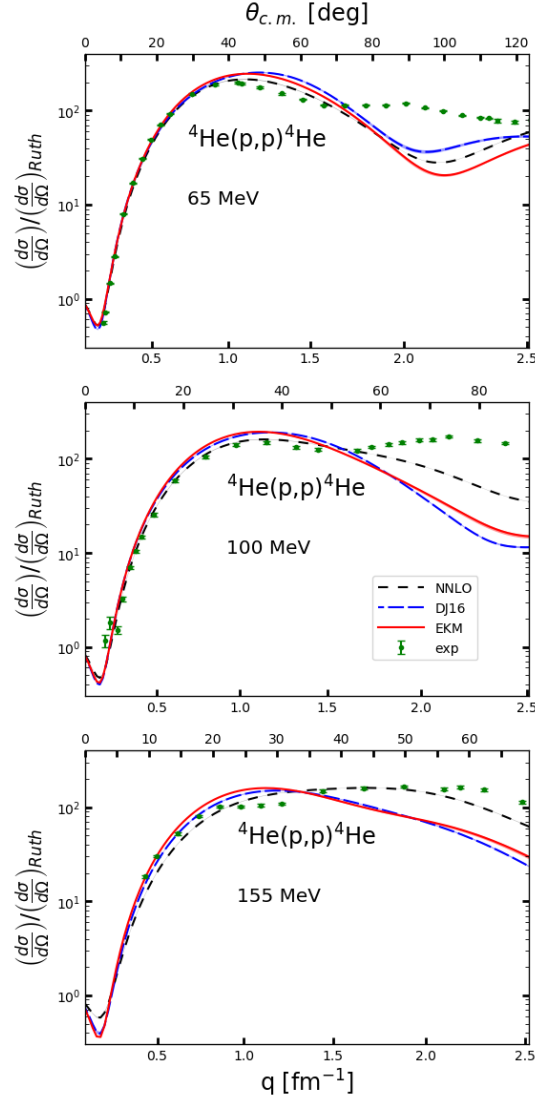


FIG. 7. The differential cross section divided by the Rutherford cross section for proton scattering from ${}^4\text{He}$ at 65 MeV (top), 100 MeV (middle), and 155 MeV (bottom) calculated using the NNLO_{opt} [34] chiral potential (short-dashed), the EKM chiral potential at order N2LO [4, 5] (solid), and the Daejeon16 potential [35] (dashed). All calculations use $N_{\text{max}} = 18$ (and 20 for the EKM potential) and $\hbar\omega = 20$ MeV. The variation of $\hbar\omega$ from 16 MeV to 24 MeV for the NNLO_{opt} and EKM and from 15 MeV to 25 MeV for the Daejeon16 structure calculations are indicated by the bands. The experimental data at 65 MeV are from Refs. [79], at 100 MeV from [80] and at 155 MeV from [81].

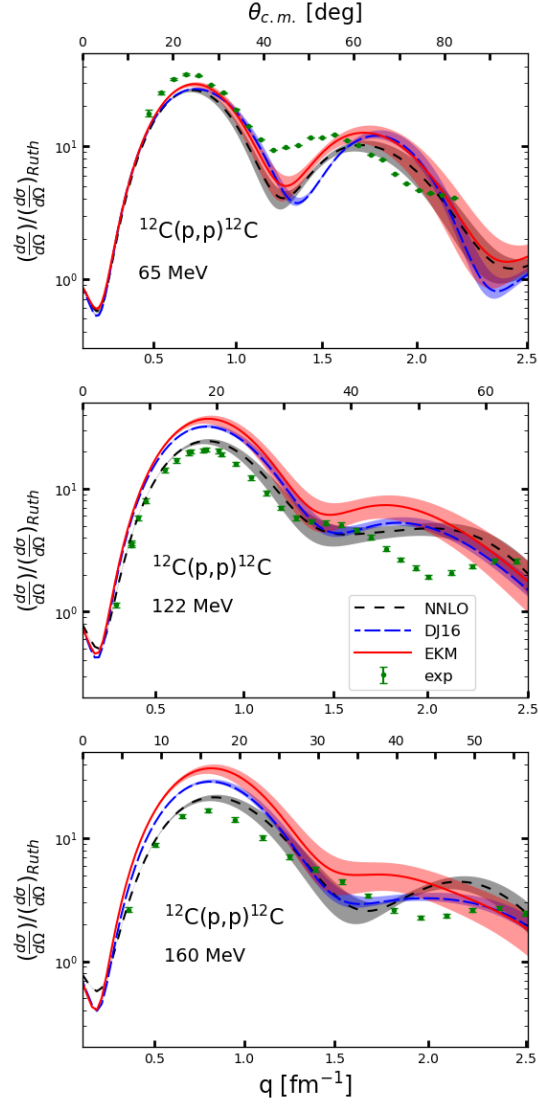


FIG. 8. The differential cross section divided by the Rutherford cross section for proton scattering from ^{12}C at 65 MeV (top), 122 MeV (middle), and 160 MeV (bottom) calculated using the NNLO_{opt} [34] chiral potential (short-dashed), the EKM chiral potential at order N2LO [4, 5] (solid), and the Daejeon16 potential [35] (dashed). All calculations use $N_{\text{max}} = 10$. The lines indicate the value of $\hbar\omega = 20$ MeV, while the bands characterize the variation of $\hbar\omega$ from 16 MeV to 24 MeV for the NNLO_{opt} and EKM, and from 15 MeV to 25 MeV for the Daejeon16 structure calculations. The experimental data at 65 MeV are from Refs. [82] and [83], at 122 and 160 MeV from [84].

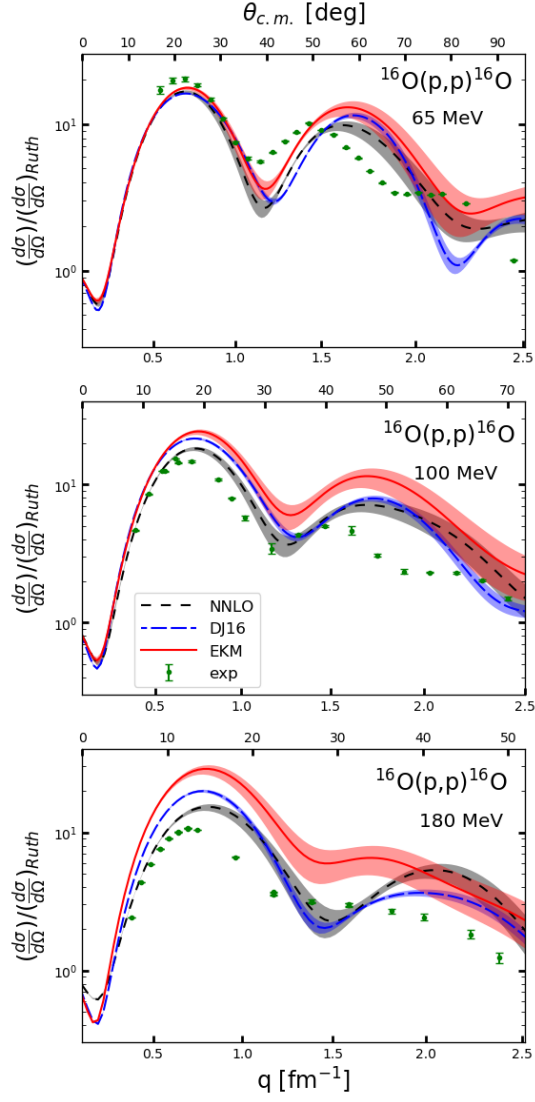


FIG. 9. The differential cross section divided by the Rutherford cross section for proton scattering from ^{16}O at 65 MeV (top), 100 MeV (middle), and 180 MeV (bottom) calculated using the NNLO_{opt} [34] chiral potential (short-dashed), the EKM chiral potential at order N2LO [4, 5] (solid), and the Daejeon16 potential [35] (dashed). All calculations use $N_{\text{max}} = 10$. The lines indicate the value of $\hbar\omega = 20$ MeV. The bands characterize the variation of $\hbar\omega$ from 16 MeV to 24 MeV for the NNLO_{opt} and EKM, and from 15 MeV to 22.5 MeV for the Daejeon16 structure calculations. The experimental data at 65 MeV are from Ref. [85] at 100 MeV from [86] and at 180 MeV from [87].

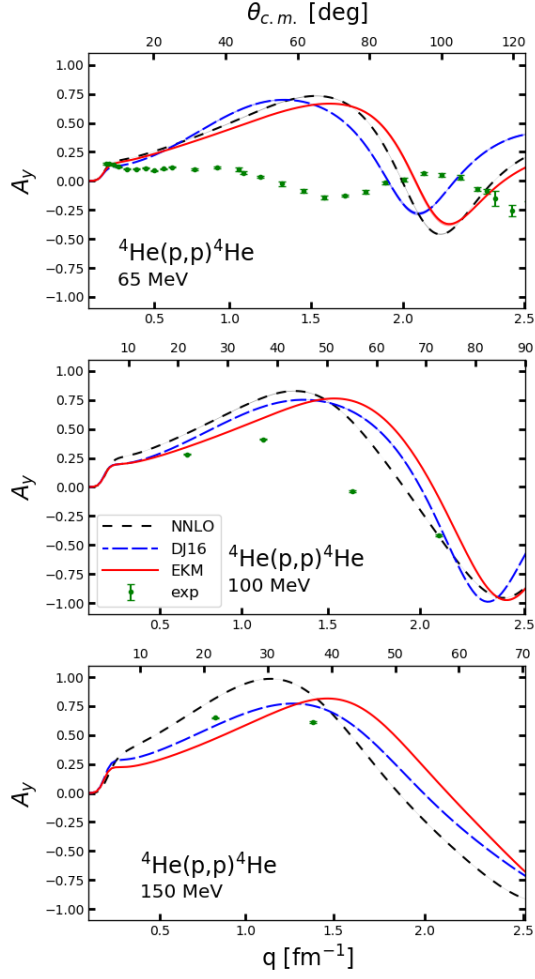


FIG. 10. The analyzing power A_y for proton scattering from ${}^4\text{He}$ at 65 MeV (top), 100 MeV (middle), and 150 MeV (bottom) calculated using the NNLO_{opt} [34] chiral potential (short-dashed), the EKM chiral potential at order N2LO [4, 5] (solid), and the Daejeon16 potential [35] (dashed). All calculations use $N_{\text{max}} = 18$ for NNLO_{opt} and Daejeon16 potentials, and $N_{\text{max}} = 20$ for the EKM potential. The lines indicate the value of $\hbar\omega = 20$ MeV. The bands characterize the variation of $\hbar\omega$ from 16 MeV to 24 MeV for the NNLO_{opt} and EKM, and from 15 MeV to 25 MeV for the Daejeon16 structure calculations. The experimental data at 65 MeV are from Ref. [79] at 100 MeV and 150 MeV from [88].

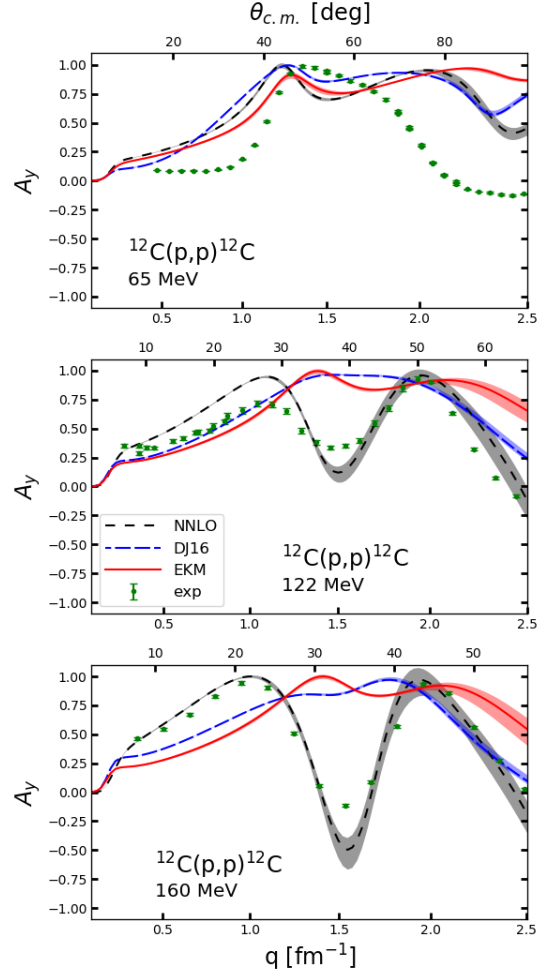


FIG. 11. The analyzing power A_y for proton scattering from ^{12}C at 65 MeV (top), 122 MeV (middle), and 160 MeV (bottom) calculated using the NNLO_{opt} [34] chiral potential (short-dashed), the EKM chiral potential at order N2LO [4, 5] (solid), and the Daejeon16 potential [35] (dashed). All calculations use $N_{\text{max}} = 10$. The lines indicate the value of $\hbar\omega = 20$ MeV. The bands characterize the variation of $\hbar\omega$ from 16 MeV to 24 MeV for the NNLO_{opt} and EKM, and from 15 MeV to 25 MeV for the Daejeon16 structure calculations. The experimental data at 65 MeV are from Ref. [89] at 122 MeV and at 160 MeV from [84].

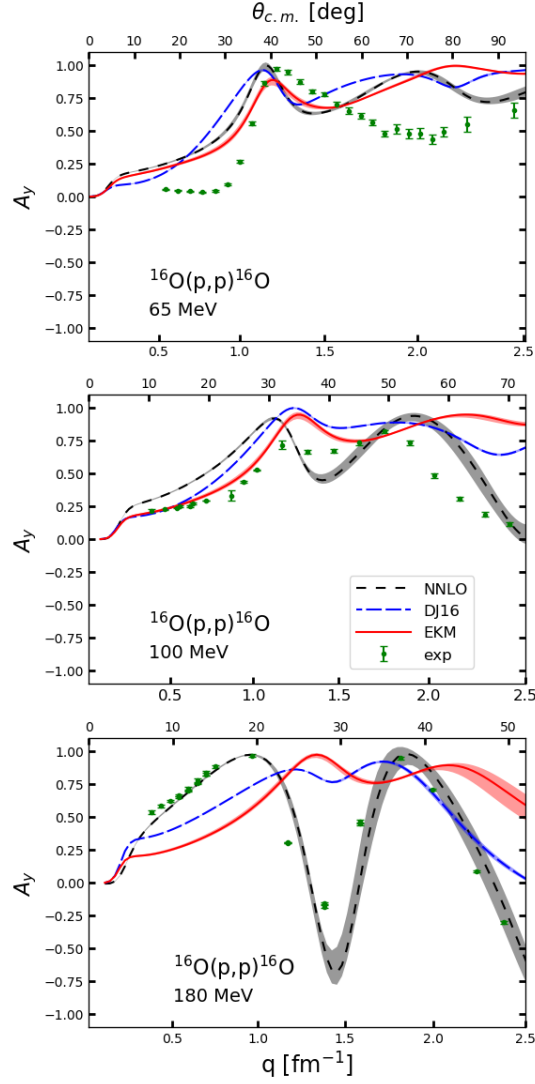


FIG. 12. The analyzing power A_y for proton scattering from ^{16}O at 65 MeV (top), 100 MeV (middle), and 180 MeV (bottom) calculated using the NNLO_{opt} [34] chiral potential (short-dashed), the EKM chiral potential at order N2LO [4, 5] (solid), and the Daejeon16 potential [35] (dashed). All calculations use $N_{\text{max}} = 10$. The lines indicate the value of $\hbar\omega = 20$ MeV. The bands characterize the variation of $\hbar\omega$ from 16 MeV to 24 MeV for the NNLO_{opt} and EKM, and from 15 MeV to 22.5 MeV for the Daejeon16 structure calculations. The experimental data at 65 MeV are from Refs. [85], at 100 MeV from [86], and at 180 MeV from [87].

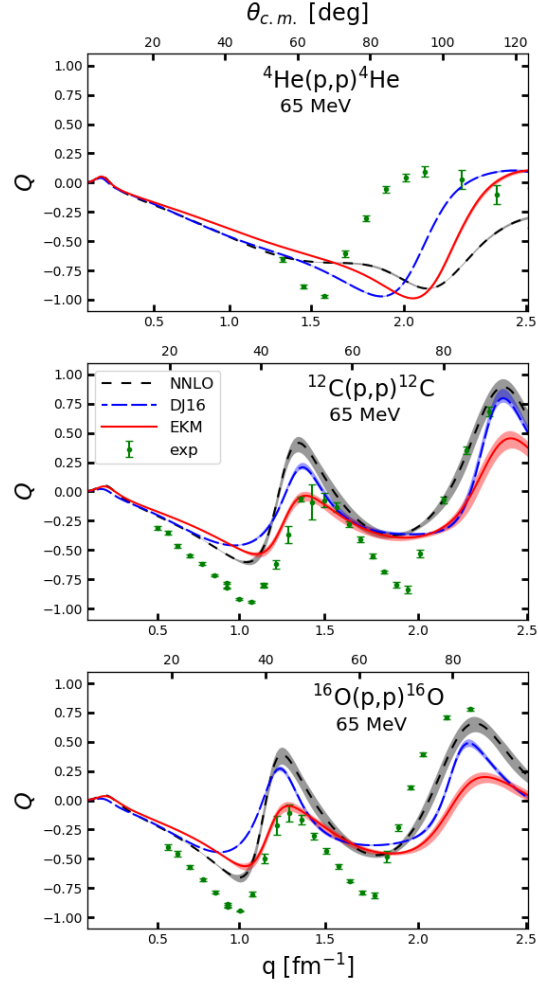


FIG. 13. The spin rotation function Q for proton scattering from ${}^4\text{He}$ (top), ${}^{12}\text{C}$ (middle), and ${}^{16}\text{O}$ (bottom) at 65 MeV calculated using the NNLO_{opt} [34] chiral potential (short-dashed), the EKM chiral potential at order N2LO [4, 5] (solid), and the Daejeon16 potential [35] (dashed). The description of the lines and bands is the same as in Figs. 6 and 8. The experimental data are from Ref. [90]

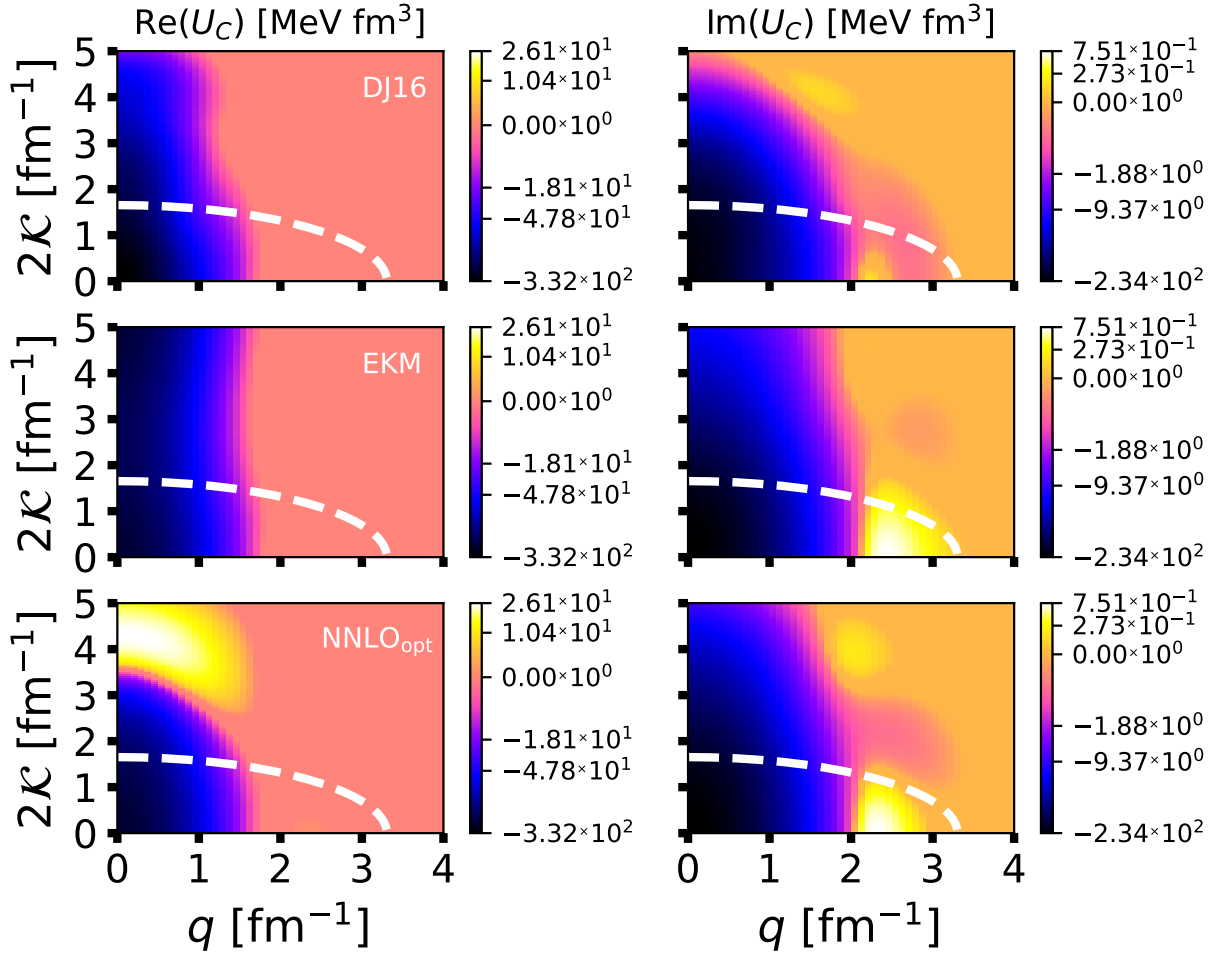


FIG. 14. The central part, $\hat{U}_C(q, \mathcal{K}, \theta_{q, \mathcal{K}})$, of the nonlocal effective interaction for proton scattering from ^{12}C at 65 MeV laboratory kinetic energy. The interaction is shown for the real (left panels) and imaginary (right panels) parts of U_C calculated from the Daejeon16 potential [35] (upper row), the EKM chiral potential at order N2LO [4, 5] (middle row), and the NNLO_{opt} [34] chiral potential (bottom row). The potentials are plotted for the angle $\theta_{q, \mathcal{K}}=90^\circ$ as functions of the momentum transfer q and the average momentum \mathcal{K} in the NA c.m. frame. The NCSM calculations use parameters $N_{\text{max}} = 10$ and $\hbar\omega = 20$ MeV in all cases. The dashed indicates the values of $U_C(q, \mathcal{K})$ for which the on-shell condition is fulfilled.

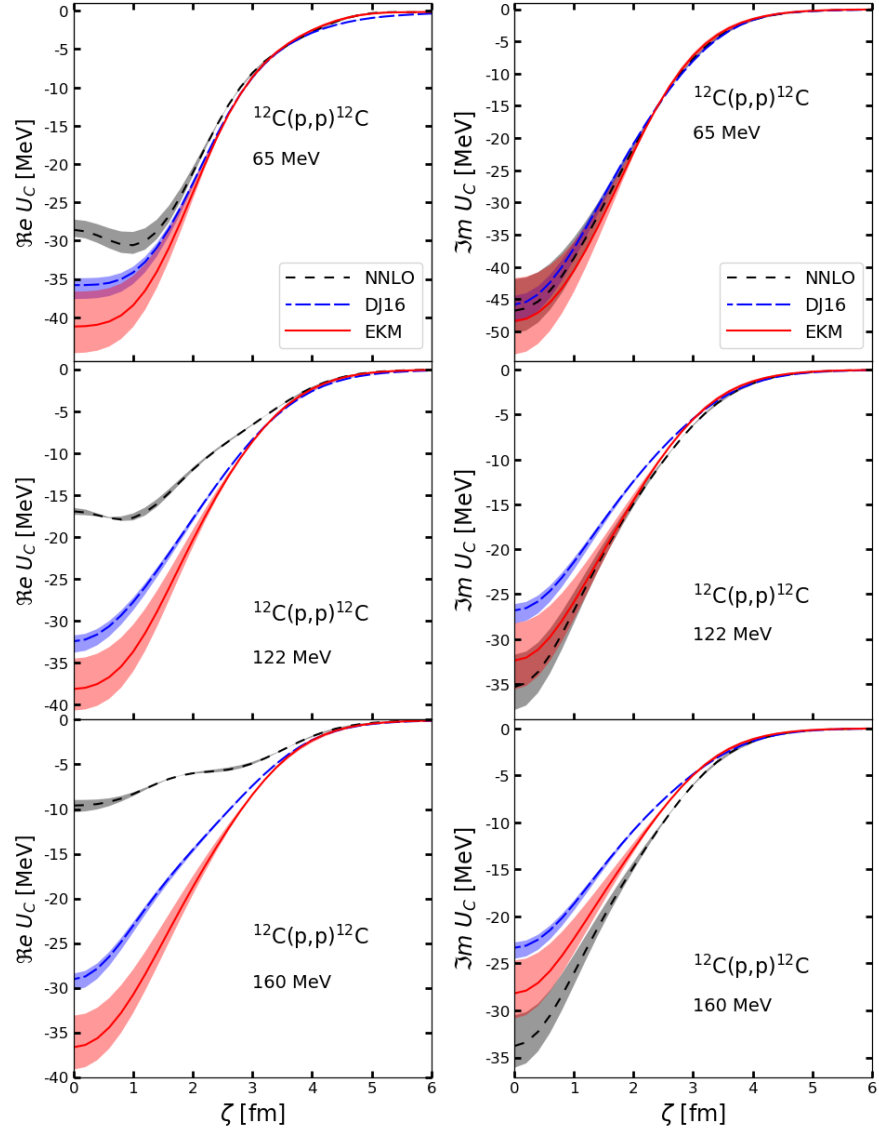


FIG. 15. The local piece of the effective central proton- ^{12}C interaction U_C as function of the radial distance extracted at 65 MeV, 122 MeV, and 160 MeV projectile energy based on the NNLO_{opt} [34] chiral potential (short-dashed), the EKM chiral potential at order N2LO [4, 5] (solid), and the Daejeon16 potential [35] (dashed). The left panel depicts the real part of U_C , while the right panel shows the imaginary part. The description of the lines and bands is the same as in Fig. 8.

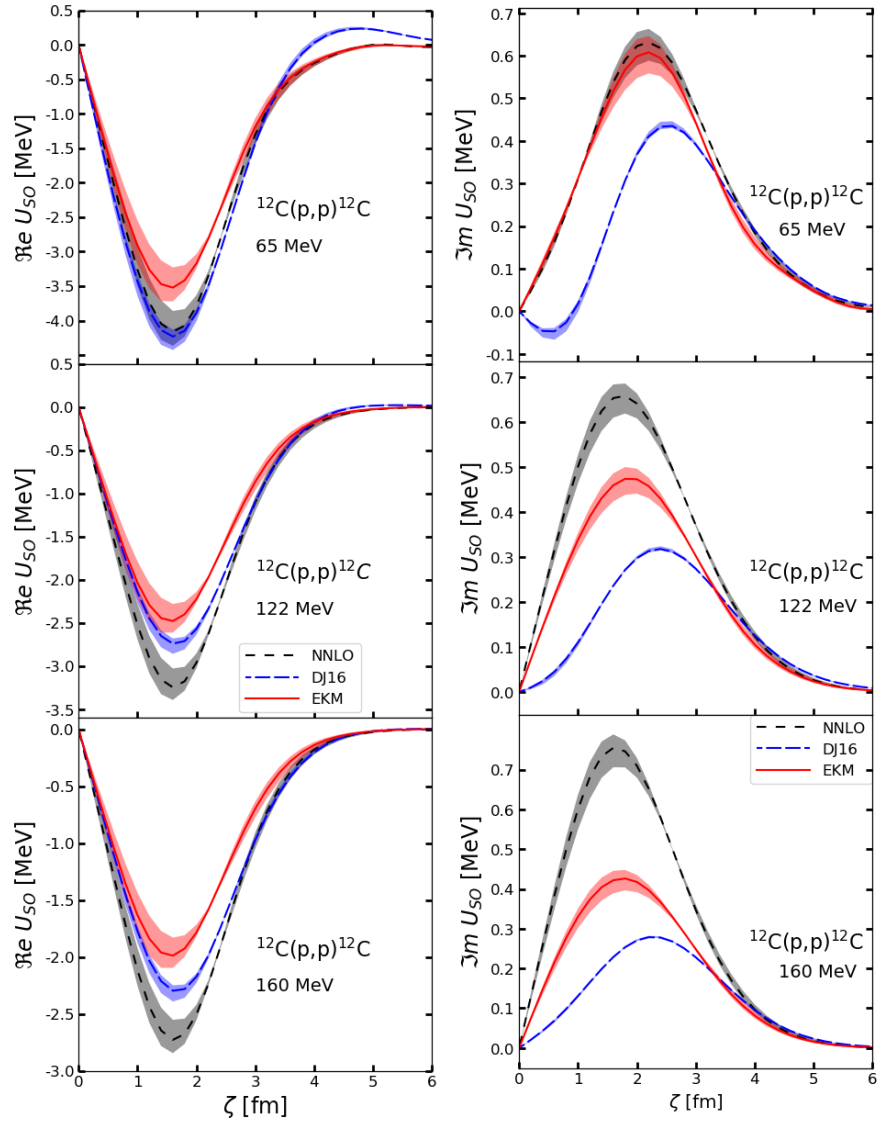


FIG. 16. The local piece of the effective spin-orbit proton- ^{12}C interaction U_{SO} as function of the radial distance extracted at 65 MeV, 122 MeV, and 160 MeV projectile energy based on the NNLO_{opt} [34] chiral potential (short-dashed), the EKM chiral potential at order N2LO [4, 5] (solid), and the Daejeon16 potential [35] (dashed). The left panel depicts the real part of U_{SO} , while the right panel shows the imaginary part. The description of the lines and bands is the same as in Fig. 8. Notice the difference in scale between the real and imaginary parts of the spin-orbit interactions.

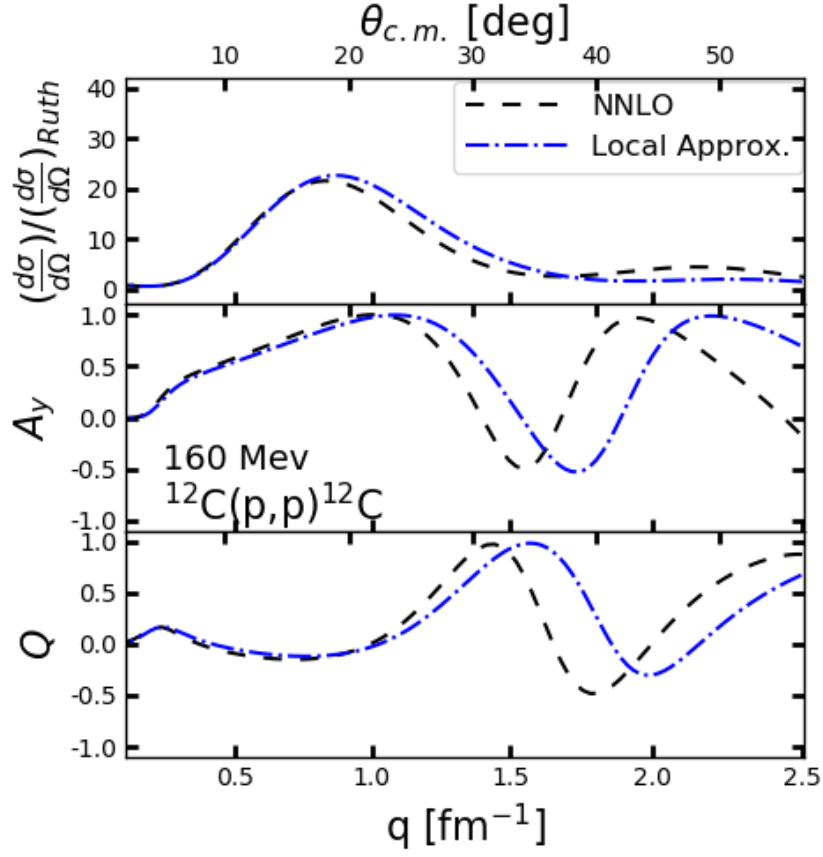


FIG. 17. The differential cross section divided by the Rutherford cross section (upper panel), the analyzing power A_y (middle panel), and the spin-rotation function Q (bottom panel) for proton scattering from ^{12}C at 160 MeV. The dashed line represents the full *ab initio* calculation based on the NNLO_{opt} [34] chiral potential using $\hbar\omega = 20$ MeV and $N_{\text{max}} = 10$, while the dash-dotted line shows the calculation based only on the local part of the corresponding effective interaction multiplied with the KMT factor. Details are given in the text.